Prospects for Incoherent Diffractive Imaging at Compact X-ray Free-electron Lasers

by

Andrew Stewart Hegeman Shevchuk

A Dissertation Presented in Partial Fulfillment
of the Requirements for the Degree
Doctor of Philosophy

Approved April 2022 by the
Graduate Supervisory Committee:

Richard A. Kirian, Chair
Kevin E. Schmidt
Uwe Weierstall
William S. Graves

ARIZONA STATE UNIVERSITY

May 2022

ABSTRACT

A time-dependent semiclassical formalism is developed for the theory of incoherent diffractive imaging (IDI), an atomically-precise imaging technique based on the principles of intensity interferometry. The technique is applied to image inner-shell X-ray fluorescence from heavy atoms excited by the femtosecond pulses of an X-ray free-electron laser (XFEL). Interference between emission from different atoms is expected when the XFEL pulse duration is shorter than the fluorescence lifetime. Simulations for atoms at the vertices of a simple icosahedral virus capsid are used to generate mock IDI diffraction patterns. These are then used to reconstruct the geometry by phase retrieval of the intensity correlation function between photons emitted independently from many different atoms at two different detector pixels. The dependence of the intensity correlation function on fluorescence lifetime relative to XFEL pulse duration is computed, and a simple expression for the visibility (or contrast) of IDI speckle as well as an upper bound on the IDI signal-to-noise ratio are obtained as a function of XFEL flux and lifetime. This indicates that compact XFELs, with reduced flux but attosecond pulses, should be ideally suited to 3D, atomic-resolution mapping of heavy atoms in materials science, chemistry, and biology. As IDI is a new technique, not much has yet been written about it in the literature. The current theoretical and experimental results are reviewed, including a discussion of signal-to-noise issues that have been raised regarding the idea that IDI is suitable for structural biology.

DEDICATION

This dissertation is dedicated to the memory of my doctoral advisor, Dr. John C. H. Spence. John's untimely passing in June 2021 ended a prodigious career advancing the fields of electron microscopy and X-ray free-electron laser science. As the scientific director of the National Science Foundation's BioXFEL Collaboration, he was instrumental to the success of the entire "diffract and destroy" paradigm of structural biology that motivated this work. The idea of using intensity interferometry at XFELs to do atomic-scale imaging genuinely excited him. Fortunately, he lived to see the original results in this dissertation accepted for publication. Thank you, John, for your guidance, patience, kindness, and inspiration.

ACKNOWLEDGMENTS

TABLE OF CONTENTS

LIST OF FIGURES

Chapter 1

INTRODUCTION

Presently, there are multiple complementary and competing techniques to image bio-logical molecules at atomic resolution for the purpose of determining their structure and dynamics. The oldest of these, X-ray crystallography, has been successfully used to determine 150,000 structures in the Protein Data Bank (Berman *et al.*, 2000), but has always had the major drawback that X-rays are ionizing and inevitably degrade any structure they are used to image. It was both proposed (Solem, 1986) and later simulated (Neutze *et al.*, 2000) that a sufficiently intense and brief pulse of X-rays could mitigate the problem of radiation damage. With the advent of next-generation X-ray sources in the form of femtosecond X-ray free-electron lasers (XFELs), the "diffraction before destruction" paradigm was born. Using XFELs, the technique of coherent diffractive imaging (CDI) developed as the primary method of structure determination. Elastically (or Bragg) scattered X-rays "outrun" the radiation damage to form diffraction patterns that are used to resolve structures at the atomic scale and even create molecular movies.

Nonetheless, the principles of quantum theory dictate that the majority of scattered X-rays are from incoherent processes. This begs the question whether such radiation, seen as a hindrance in CDI, can also be useful in mapping atomic structures. A new technique named incoherent diffractive imaging (IDI) was proposed by Classen *et al.* (2017) that uses these incoherent photons—specifically in the form of K-shell X-ray fluorescence of transition metal atoms—to resolve atomic structures. In an IDI experiment, an XFEL pulse is tuned to a frequency just above the ionization energy of the inner electron shell of a target element in a sample. The atom then fluoresces when hit by the X-ray beam, emitting a lower-energy

X-ray isotropically. Normally these X-ray fluorescent photons are background noise in a CDI experiment, but if pairs of fluorescent photons are detected on a timescale comparable to the fluorescence coherence time, they will interfere with each other and form a speckle pattern. The correlations in the detected fluorescence contain structural information about the relative position of the emitting atoms and may aid the 3D, atomically-precise imaging of biological samples. This technique of studying intensity correlations on a detector array between incoherent photons is characteristic of intensity interferometry experiments pioneered by Robert Hanbury Brown and Richard Q. Twiss in the 1950s. Indeed, IDI is an XFEL-adapted application of the principles of intensity interferometry to achieve atomic-resolution imaging.

The rest of this introductory chapter establishes the basic functionality of XFELs and compact XFELs, the method of CDI, and the principles of intensity interferometry that underlie IDI. Intensity interferometry works both at the classical and quantum levels, with the observation of enhanced correlation between seemingly independent photons now known as the Hanbury Brown and Twiss (HBT) effect, a fundamental result in quantum optics. The basic mathematics of intensity interferometry is outlined and the work of HBT and its relation to IDI are discussed.

In the second chapter, an overview of the current literature on the subject of IDI is presented. As the technique is so new, having been first formally proposed all of five years ago, there has not yet been a robust experimental demonstration that IDI will work in practice. Furthermore, there are important theoretical questions surrounding the signal-to-noise ratio (SNR) in an IDI experiment that are a focus of the literature. We review both the SNR discussions and the current experimental progress in realizing IDI so that the reader may be informed on the status of this technique and some of the opportunities and difficulties it presents.

The third chapter details the author's original contribution to the field (Shevchuk *et al.*, 2021), showing with a time-dependent semiclassical model that the SNR scales favorably in the case of IDI if the pulse duration is comparable to or less than the coherence time of the fluorescence. It remains to focus the X-ray beam to boost the ionization rate to an average of one event per potential emitter per pulse, which can be done with Laue lenses. This result is especially important for the viability of IDI using compact XFELs, an upcoming generation of machines that can produce attosecond pulses at the cost of reducing the pulse intensity orders of magnitude beneath that possible at a larger XFEL. The pulse intensity constraint makes the standard paradigm of CDI rather difficult to realize at a compact XFEL, so new techniques are needed to take advantage of these machines' capabilities. These results show IDI is best suited for the capabilities of a compact XFEL. However, the SNR considerations reviewed in Chapter 2 may still pose limitations on what might be accomplished even at compact XFELs, especially for biomolecular samples where the density of emitters tends to be quite low. The dissertation concludes by noting that the full story around IDI is still developing and that the ultimate arbiter for the technique as envisioned—a quintessential experiment demonstrating that IDI can feasibly image a biological sample in 3D at the atomic scale—is still in the future.

1.1   X-ray Free-electron Lasers

X-ray free-electron lasers provide coherent femtosecond-scale X-ray pulses with a brilliance at least an order of magnitude beyond the brightest synchrotron sources. They achieve this by accelerating bunches of electrons to nearly the speed of light and passing them through an undulator, a region of rapidly alternating magnetic fields. The acceleration causes the electrons to emit X-rays, which continue to modulate the electron beam, sorting

it into coherent bunches separated by the wavelength of the radiation. This enforces the production of further X-rays at the same wavelength and phase, creating "microbunches" and a positive feedback loop. This high-gain mode, known as self-amplified spontaneous emission (SASE), achieves a spatially coherent X-ray pulse of femtosecond duration at an intensity approaching 10^{12} photons at large XFEL facilities. A variety of XFELs operating via SASE have been built. The first soft XFEL was FLASH, built at DESY in Hamburg, Germany in 2005 and the first hard XFEL was the Linac Coherent Light Source (LCLS), built at the SLAC National Accelerator Laboratory in Menlo Park, California in 2009. Since then nearly a dozen hard XFELs have been built across the world.

Figure 1. CXFEL design

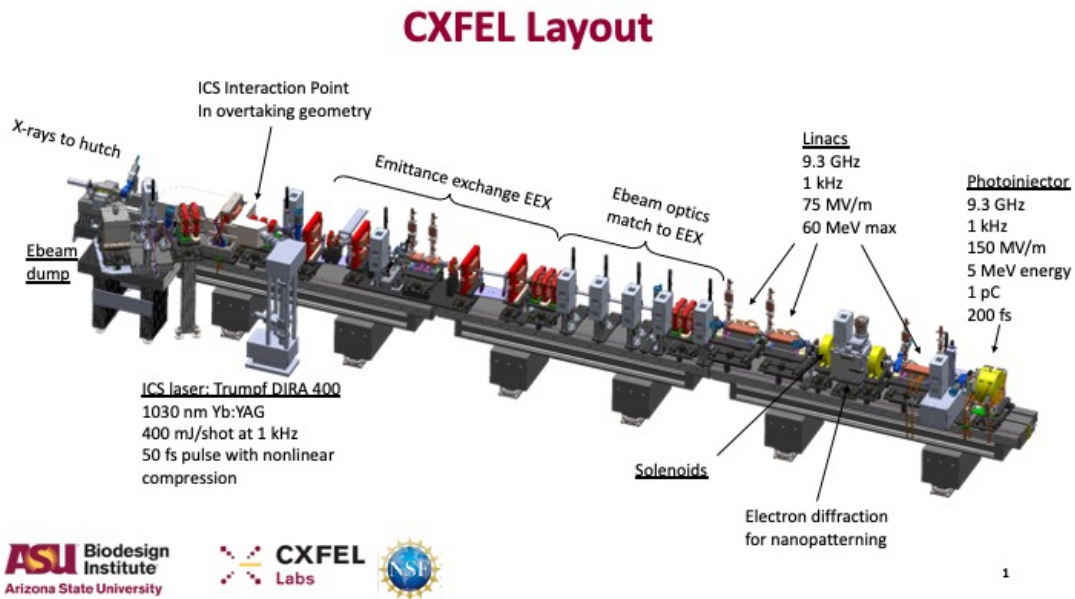The layout of the compact XFEL built at the Arizona State University is shown, with the X-ray beam traveling from right to left.

A new generation of smaller machines that do not rely on SASE to function, known as compact XFELs, is now under construction. The first of these is the ten-meter long CXFEL (see Figure 1), located at Arizona State University (Graves *et al.*, 2017). CXFEL replaces the

4

undulators used at large XFELs with a short-pulse laser field. This leads to "nanobunching" of the electrons and is expected to produce temporally-coherent pulses <10 fs containing 10^8 photons with a pulse cadence of 1 kHz. Using beam optics, the machine can reach attosecond pulse durations while maintaining control over the phase, bandwidth, amplitude, and frequency of the pulse. This precision control enables new techniques not currently possible at SASE-based XFELs, but compact XFELs may also be used to seed SASE-based XFELs, transferring their desirable beam properties to the larger machines. The most important feature of compact XFELs for IDI is that these machines produce sub-femtosecond pulses. Since the fluorescence lifetime of K_α X-rays for transition metals is approximately half a femtosecond, a stronger correlation among fluorescence generated at a compact XFEL is expected relative to those at larger XFELs.

1.2 Coherent Diffractive Imaging

The method of coherent diffractive imaging (CDI) is shown in Figure 2. Many identical samples, which can be single molecules or crystals, are prepared and injected into the XFEL beam in rapid succession. Each XFEL pulse scatters off a sample and is recorded as a single diffraction pattern on a charge-coupled device. The X-rays photoionize the sample, generating a substantial net positive charge that blows it apart in a Coulomb explosion (hence the moniker "diffraction before destruction"). The pulse rate is synchronized to the detector readout rate so that each exposure contains at most the scattering of a single pulse. The diffraction patterns, corresponding to samples hit at a random orientation, can be divided into groups of like orientation and averaged together to suppress noise. Each of these pattern groups corresponds to a slice of the Ewald sphere, the sphere in reciprocal space on which all scattering vectors $\mathbf{q} = \mathbf{k}_{out} - \mathbf{k}_{in}$ are located for incident wavevector $\mathbf{k}_{in}$ and scat-

tered wavevector $\mathbf{k}_{out}$. Combined over all orientations of the sample, each of which defines a different Ewald sphere, the patterns fill a volume in reciprocal space that can be Fourier transformed to real space using phase retrieval techniques. This provides the charge density of the electrons surrounding the atoms, and therefore their positions.
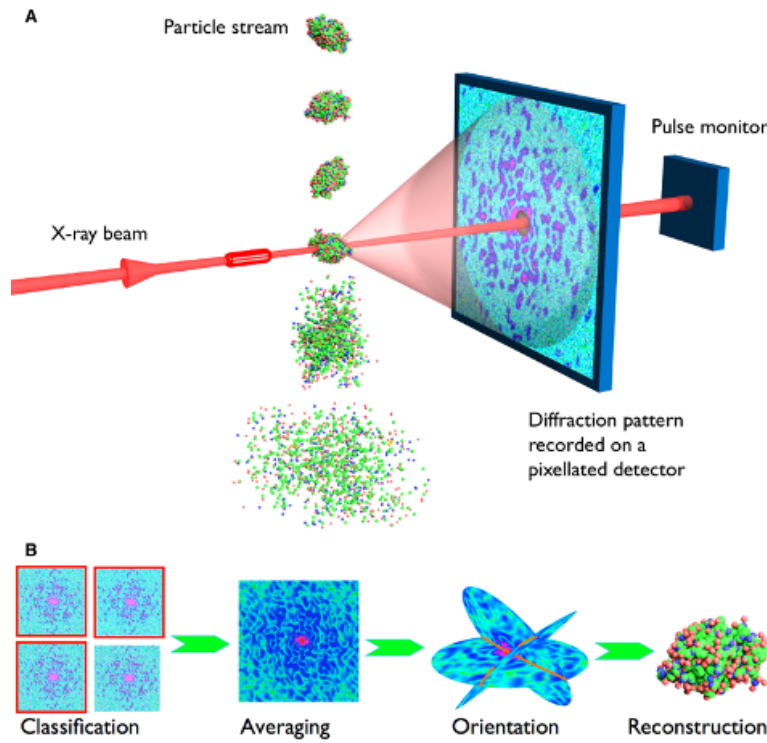
Figure 2. Coherent diffractive imaging

This figure depicts the standard implementation of the "diffraction before destruction" paradigm at XFELs. Although the schematic shows a single-particle sample, Bragg diffraction from crystals is commonly used to scatter more photons and improve the signal-to-noise ratio. Image taken from Gaffney and Chapman (2007).

For a typical crystal sample, 98% of the X-ray photons pass through without interacting. Of the remaining 2%, about 84% of these are photoabsorbed and 8% are Compton scattered. Only 8% of those that interact are Bragg scattered (Spence, 2017). This is purely a consequence of the relative sizes of the photoionization and Thomson scattering cross sections;

roughly a hundred times as many photons deposit their energy into the sample as Bragg scatter off of it. Since it cannot be avoided, it is critical to the success of the CDI method that the XFEL pulse be brief enough to outrun this radiation damage. That is, the X-rays must scatter before the atoms have moved an appreciable distance due to the ionization cascade of the Auger effect. This timescale is of femtosecond order in light elements (Campbell and Papp, 2001). Because of the difficulty of compressing more electrons into a smaller bunch, decreasing the pulse duration to a few femtoseconds or less has the trade off that the pulse intensity will be orders of magnitude lower. This makes it difficult for a compact XFEL to compete with the results achievable by large XFELs using CDI. Making use of these photoionization events was a significant motivator for developing IDI.

1.3   Intensity Interferometry

Incoherent diffractive imaging is an application of intensity interferometry. Broadly, interferometers fall in two different classes: amplitude interferometers and intensity interferometers. In amplitude interferometry, interference between two waveforms superimposed on a detector can be expressed in terms of the correlation function of their amplitudes—known as the degree of first-order coherence. The double slit experiment (see Figure 3) is the quintessential example of this; the intensity on the screen is expressible in terms of the field amplitudes of the waves diffracting through the slits. Intensity interferometry characterizes interference not at a single point on a detector, but between events at a pair of detectors. This can be expressed as a correlation function of the intensities measured in the two detectors—the degree of second-order coherence, which is fourth-order in the amplitudes. Both cases are related to each other and are examined below.

Consider a static plane wave $E(r)$ of light incident on two diffraction slits a and
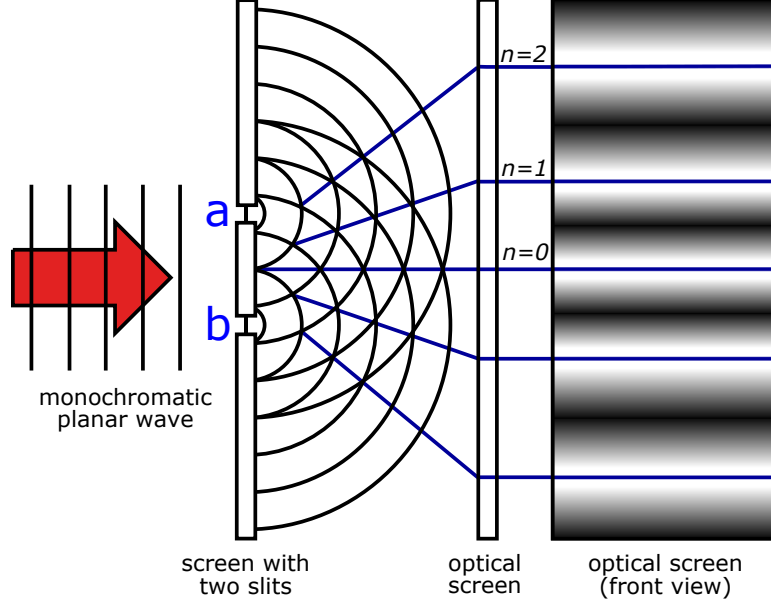
Figure 3. The classic double-slit experiment

b. These slits produce time-independent spherical waves $E_a e^{ik|\mathbf{r}-\mathbf{r}_a|+i\phi_a}/|\mathbf{r} - \mathbf{r}_a|$ and $E_b e^{ik|\mathbf{r}-\mathbf{r}_b|+i\phi_b}/|\mathbf{r} - \mathbf{r}_b|$ emanating from slits a and b respectively. Here E_a and E_b are purely imaginary, as the diffraction slit rotates the wave $\pi/2$ radians out of phase with the incident light (Loudon, 1973). Take the far-field limit where the slits are a distance $L >> (r_b - r_a)$ from the screen. The intensity at a point on the screen is expressed as

$$
\begin{aligned}
I(\mathbf{r}) &= \frac{1}{L^2}(|E_a|^2 + |E_b|^2 + E_a^* E_b e^{i(k(r_b-r_a)+\phi_b-\phi_a)} + E_a E_b^* e^{-i(k(r_b-r_a)+\phi_b-\phi_a)}) \quad (\text{1.1}) \\
&= I_a + I_b + \frac{2}{L^2}\mathrm{Re}[E_a^* E_b e^{i(k(r_b-r_a)+\phi_b-\phi_a)}] = I_a + I_b + 2\sqrt{I_a I_b}\mathrm{Re}[g^{(1)}].
\end{aligned}
$$

The last term, characterizing the interference of the amplitudes, contains the (normalized) complex degree of first-order coherence of the radiation. For the static case being considered, it takes the form $g^{(1)} = \langle E^*(r_a)E(r_b)\rangle/\sqrt{I_a I_b} = |g^{(1)}|e^{i(k(r_b-r_a)+\phi_b-\phi_a)}$.

It is important to distinguish temporal coherence and spatial coherence in $g^{(1)}$. The degree of temporal coherence describes any time-evolution in the relative phases of the light through the slits. If the path length difference to the screen is large enough between the two

slits, the light will become incoherent because its relative phase has appreciatively evolved by the time it is detected. The degree of spatial coherence describes features of the light field not due to the evolution of the relative phases in time. This can refer to changing the angular size of the source, changing the wavelength of the light, or changing the separation of the slits without introducing a path length difference. Since the treatment here is time-independent, the waves are automatically temporally coherent, with the pattern of maxima and minima across the screen characterizing the spatial coherence.

Temporal coherence is quantified by the visibility function (or contrast), defined as

$$\mathcal{V}_{amp} = \frac{I_{max} - I_{min}}{I_{max} + I_{min}} = \frac{2\sqrt{I_a I_b}|g^{(1)}(\tau)|}{I_a + I_b} \tag{1.2}$$

where τ refers to the difference in time it takes radiation to reach a point on the screen from each slit. In the static case it is a constant and the fringes do not decay as one moves horizontally along the screen. In a real experiment the contrast diminishes at higher order maxima, reflecting the loss of temporal coherence.

There is clear structural information in the value of $g^{(1)}$, including information about the separation of the slits $r_b - r_a$ as well as the relative phase information. If the phases are averaged over all possible initial values, then the correlation term vanishes and only $\langle I \rangle = I_a + I_b$ remains, that is, the average intensity is just a constant sum of the individual intensity contributions of each slit. The structural information is then lost. Moreover, the visibility function modulates the amplitude of this signal, so it is desirable to maximize it however possible.

In practice, it may not be easy to measure $g^{(1)}$ directly. For example, the Michelson interferometer uses a system of paired mirrors to direct starlight into a focal plane where it forms fringes on a screen. The fringes translate on the screen when a path length difference of order the wavelength of the light is introduced between the arms of the interferometer. If this occurs rapidly at random, it blurs the fringes and decreases their visibility. This require-

ment of rigidity on a scale smaller than the wavelength of light is characteristic of amplitude interferometers, so they are difficult to operate at X-ray wavelengths.

Instead of a single detector (screen), consider intensities I_A and I_B measured in a pair of detectors A and B, which can themselves be part of an array of detectors like each individual pixel on a charge-coupled device. If the light now emanates from two independent emitters a and b and is incident on both of these detectors, the product of these intensities can be computed:

$$
\begin{aligned}
I_A I_B = {} & I_{Aa} I_{Ba} + I_{Ab} I_{Ba} + I_{Aa} I_{Bb} + I_{Ab} I_{Bb} \\
& + 2(I_{Aa} + I_{Ab}) \sqrt{I_{Ba} I_{Bb}} \cos \left(k(r_{Bb} - r_{Ba}) + \phi_b - \phi_a \right) \\
& + 2(I_{Ba} + I_{Bb}) \sqrt{I_{Aa} I_{Ab}} \cos \left(k(r_{Ab} - r_{Aa}) + \phi_b - \phi_a \right) \\
& + 4 \sqrt{I_{Aa} I_{Ab} I_{Ba} I_{Bb}} \cos \left(k(r_{Bb} - r_{Ba}) + \phi_b - \phi_a \right) \cos \left(k(r_{Ab} - r_{Aa}) + \phi_b - \phi_a \right).
\end{aligned} \tag{1.3}
$$

Here r_{Aa} represents the distance from emitter a to detector A, and I_{Aa} is the corresponding contribution of the light from emitter a to detector A's measured intensity. Since the emitters are independent, the photons are produced with random phases (although the phases themselves do not evolve as the light propagates). This random nature of the phases of the photons produced by the emitters defines chaotic light. Averaging over the possible phases results in

$$
\langle I_A I_B \rangle = \langle I_A \rangle \langle I_B \rangle + 2 \sqrt{I_{Aa} I_{Ab} I_{Ba} I_{Bb}} \cos \left(k(r_{Bb} - r_{Ba} - r_{Ab} + r_{Aa}) \right). \tag{1.4}
$$

The last term is due to $\overline{\operatorname{Re} \mathcal{A} \times \operatorname{Re} \mathcal{B}} = \frac{1}{2} \operatorname{Re}(\mathcal{A} \mathcal{B}^*)$, the "cycle-average" identity for complex quantities $\mathcal{A}$ and $\mathcal{B}$. In the far-field approximation, $k(r_{Bb} - r_{Ba} - r_{Ab} + r_{Aa})$ factors into $k(\hat{\mathbf{r}}_B - \hat{\mathbf{r}}_A) \cdot (\mathbf{r}_b - \mathbf{r}_a) = (\mathbf{k}_B - \mathbf{k}_A) \cdot (\mathbf{r}_b - \mathbf{r}_a)$ for $\mathbf{k}_i = k \hat{\mathbf{r}}_i$ the wavevector into detector i. Identifying detector separation $\mathbf{q} = \mathbf{k}_B - \mathbf{k}_A$ and normalizing by $\langle I_A \rangle \langle I_B \rangle$, then the degree of second-order coherence is

$$g^{(2)}(\mathbf{q}) = \frac{\langle I_A I_B \rangle}{\langle I_A \rangle \langle I_B \rangle} = 1 + \frac{2\sqrt{I_{Aa}I_{Ab}I_{Ba}I_{Bb}}}{\langle I_A \rangle \langle I_B \rangle} \cos\left(\mathbf{q} \cdot (\mathbf{r}_b - \mathbf{r}_a)\right). \tag{1.5}$$

By substituting $I = \langle I \rangle + \Delta I$, the latter term corresponds to the magnitude of the correlation between intensity fluctuations:

$$\frac{\langle \Delta I_A \Delta I_B \rangle}{\langle I_A \rangle \langle I_B \rangle} = \frac{2\sqrt{I_{Aa}I_{Ab}I_{Ba}I_{Bb}}}{\langle I_A \rangle \langle I_B \rangle} \cos\left(\mathbf{q} \cdot (\mathbf{r}_b - \mathbf{r}_a)\right). \tag{1.6}$$

Comparing this with the amplitude interferometry results, the coefficients have the structure of a product of first-order visibility functions and will be referred to as the visibility $\mathcal{V}$ of the intensity correlation in subsequent sections. Per the far-field geometry of the experiment and ignoring the dot product so that only the projected separation is considered (which is automatically the case for a double-slit experiment as the slits are parallel to the screen), $|\mathbf{r}_b - \mathbf{r}_a| = \theta/L$ for a source separation of angular size θ. Identifying a detector separation $d \approx L|\hat{\mathbf{r}}_B - \hat{\mathbf{r}}_A|$, the last term is proportional to $\cos\left(2\pi\theta d/\lambda\right)$. By adjusting the detector separation d until the magnitude of the correlation vanishes, the angular separation of the sources (in projection) can be determined. This characterizes the spatial coherence of the light field and is precisely what Hanbury Brown and Twiss did in the 1950s (Brown and Twiss, 1954). They built a correlator that multiplied the output currents of a pair of detectors and observed a correlation in the intensity fluctuations of those currents. By adjusting the detector separation until this correlation vanished and integrating over all possible orientations of the source (i.e., letting the Earth rotate with respect to the sky), they were able to measure the angular diameter of the star Sirius A (Brown and Twiss, 1956).

Their result was initially controversial on account of the quantum nature of light (Goodman *et al.*, 1997). While there was no dispute that there exists an intensity correlation in the wave interpretation of light (as demonstrated above), quantum electrodynamics was a relatively new theory at the time and interpreting the interference of seemingly independently-

generated and detected photons was not well understood, especially since photons—being uncharged—are not expected to interact with each other in a quantum field theory. The quantum interpretation can be understood as purely a statistical effect associated to the uncertainty principle. As shown by Figure 4, the photons can be jointly detected in two ways. Either a photon from a is detected at A and a photon from b is detected at B, or one from a is detected at B and one from b is detected at A. If these two possibilities are indistinguishable to the observer, that is, if the detection occurs with a geometry and timeframe where either outcome is possible, then the photons will be coherent and interfere with each other via their intensity correlation. If the two possibilities are distinguishable to the observer, the correlation will not appear.

Distinguishability may be possible, for example, because the energy difference between the photons is resolvable. Such a difference creates a beat mode between the two photons of frequency $\omega_b - \omega_a$. Although it is not readily apparent in the static formalism used here, a major advantage of intensity interferometry is that the correlation is only sensitive to changes in the relative path lengths through the instrument of order the wavelength of the *beat*, not to the wavelength of the light itself. This is one advantage over amplitude interferometers that made HBT's measurements possible. They used an optical filter of 450 ± 5 nm and an electronic filter to remove all frequencies above 10^8 Hz, so only beat frequencies smaller than that would reach the correlator. At 10^8 Hz, their instrument could tolerate a path length difference of about 30 cm without appreciatively disrupting the relative phase of the light and destroying the coherence. Unlike the Michelson interferometer, the beat wavelength is not nearly as limiting an engineering requirement, at least at optical wavelengths.

One disadvantage readily apparent in the treatment provided above is that all information about the relative phase of the light is lost to the observer in an intensity interferometer. It is averaged out, whereas this is not true in amplitude interferometry. Therefore, to obtain
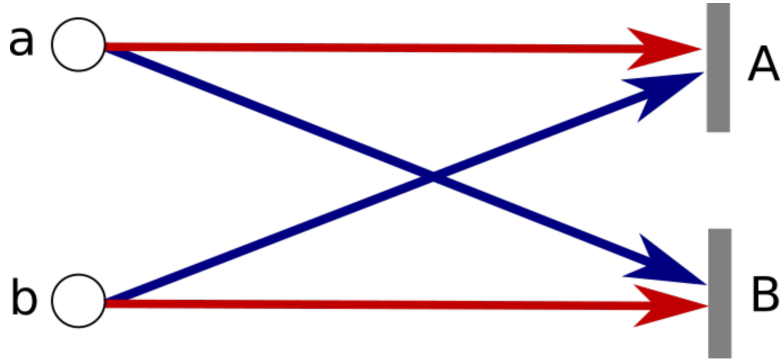
Figure 4. Photon pairs in intensity interferometry experiments

How can the measurements of two photons be correlated if they are both emitted and detected independently of each other? The uncertainty principle forces the observer to trade resolution in time for resolution in energy. If photons emitted at a and b with frequency difference $\Delta\omega$ (in this case the fluorescence linewidth) have optical path differences to each of detectors A and B within a time $\Delta\tau_c$ of each other, the observer cannot distinguish the photons when $\Delta\omega\Delta\tau_c < 1/2$. Consequently, the two photons could have taken either set of colored paths in the image to arrive at the detectors, and so are coherent and briefly produce interference fringes. Each path arriving at a detector considered in isolation only contributes to the homogeneous background (since this definitively selects whether the red or the blue paths were followed). Only when the paths are considered as pairs, meaning the joint probability of detecting the photons is considered, does the interference emerge, and with it the ability to extract structural information from the correlation function. Note that this picture only makes sense in the far-field limit, where the spatial modes are indistinguishable.

a 3D reconstruction of the emitter geometry, intensity interferometry has to solve a "phase problem" analogous to that familiar in coherent X-ray diffraction experiments. Another disadvantage of HBT's method is that they relied on an electronic correlator to integrate the signal. Not only is the path length difference through both the optics and electronics significant to maintaining coherence between the signals, but the detector and electronics have a characteristic response time that adversely impacts the temporal coherence of the light. The visibility of the correlations is reduced by needing to average over this response time, which for HBT's experiment reduced the visibility to the order of 10^{-5}.

An IDI experiment is complementary, in some sense, to the experiments done by HBT.

The role of the star can be substituted with that of the sample and the idea of averaging over time can be replaced by a statistical average over many diffraction patterns, but a key difference is that the correlator—which compares signals at the end of the opto-electronic path in an HBT experiment—is functionally replaced by the XFEL pulse at the beginning of the path in an IDI experiment. In both cases, there is a characteristic timescale that gates the signal. For HBT it is the response time of the detection system while for IDI it is the duration of the XFEL pulse. In each case this timescale must be averaged over to yield the final visibility seen by an observer.

Having the gating mechanism *before* the incoherent photons are generated rather than after they are detected makes intensity interferometry possible at X-ray energies. Since, in an HBT setup, the relative path length difference matters through the entire optical *and* electronic system up to the correlator, and that difference must be shorter than the wavelength associated to the beat frequency of the photon pair, the precision required to do the experiment becomes extremely difficult to engineer at high beat frequencies. Transferring the function of the correlator to the XFEL beam permits the experimenter to simply use standard integrating detectors (in fact, each pixel in the detector array qualifies as a "detector" in the sense of HBT). While the experimental geometry still dictates where the detectors must be placed (the constraint of minimizing the relative path length difference still applies), nothing about this design requires that the experiment must be done at X-ray energies, suggesting that IDI can be performed at longer wavelengths as well.

Chapter 2

A REVIEW OF IDI THEORY AND EXPERIMENTS

The original idea for IDI was proposed and simulated by Classen *et al.* (2017). In their fully-quantum formalism they generalized the time-independent treatment of intensity interferometry in the previous chapter to use an array of emitters and detectors. They considered a series of N_E identical point-like emitters with distribution $S(\mathbf{r}) = \sum_i^{N_E} \delta(\mathbf{r} - \mathbf{r}_i)$. The Fourier transform of this quantity,

$$\tilde{S}(\mathbf{q}) = \sum_i^{N_E} e^{i\mathbf{q}\cdot\mathbf{r}_i}, \tag{2.1}$$

is the structure factor in crystallography. Computing the degree of second-order coherence, they established that

$$g^{(2)}(\mathbf{q})_{TLS} = |\tilde{S}(0)|^2 + |\tilde{S}(\mathbf{q})|^2 = 1 + |g^{(1)}(\mathbf{q})|^2 \tag{2.2}$$

where $g^{(1)}(\mathbf{q}) = \tilde{S}(\mathbf{q})/\tilde{S}(0)$—the spatial part of the complex degree of first-order coherence—is just the normalized structure factor and "TLS" stands for "thermal light source" emitters. Equation (2.2) is known as the Siegert relation and holds generally in the limit of a large number of emitters. In the case when the emission is only partially temporally coherent, the expression should be adjusted (per Trost *et al.* (2020)) to

$$g^{(2)}(\mathbf{q})_{TLS} = 1 + \mathcal{V}|g^{(1)}(\mathbf{q})|^2 \tag{2.3}$$

with the visibility $\mathcal{V}$ containing the time-dependent part of $g^{(1)}$. The thermal limit is useful for a number of simplifications, but in the context of X-ray fluorescence only one K_α photon per emitter is expected. A more accurate expression derived by Classen *et al.* (2017) (again with the partially coherent modification by Trost *et al.* (2020)) for single-photon emitters

(SPEs) is

$$g^{(2)}(\mathbf{q})_{SPE} = 1 + \mathcal{V}(-2/N_E + |g^{(1)}(\mathbf{q})|^2). \qquad (2.4)$$

The extra term vanishes in the thermal limit $N_E \to \infty$ and the factor of two accounts for the inability of the atom to emit a second photon (that could create intensity correlations with the first) within the coherence time of the fluorescence.

Classen *et al.* (2017) identify several features of IDI that they see as advantages over CDI. They note, as previously mentioned, that the cross sections of photoionization are significantly larger than those of elastic scattering and that the fluorescence is emitted isotropically, whereas the intensity in CDI decreases as $\mathbf{q}^{-4}$ for small values of $\mathbf{q}$. Also, high dynamic range requirements for the detectors are not necessary as the concentration of many photons into Bragg peaks only occurs when analyzing the photon correlations, not when detecting the photons themselves. The method is also chemically specific as the targeting of K_α emission with the XFEL beam energy selects for fluorescence from a particular element.

Interestingly, IDI permits genuine 3D imaging because the $\mathbf{q}$-vectors are not measured relative to the incident beam as they are in CDI, but between any two pixels on the detector. This breaks the restriction imposed by the elastic scattering condition that $\mathbf{q}$ is located on the Ewald sphere. Instead, $\mathbf{q}$-vectors fill a volume in the reciprocal space even if the detector is flat in real space. A hypothetical spherical detector in real space would provide information about an entire spherical volume of magnitude $|\mathbf{q}_{max}|$ in reciprocal space. As $\mathbf{q}_{max}$ spans the diameter of such a detector, its magnitude is twice that possible in the case of CDI, and this suggests that a large amount of structural information may be obtainable from relatively few diffraction patterns with the statistics of a large number of possible pixel pairings.

While a pulse duration comparable to τ_c (the coherence time of the fluorescence) is optimal, the method also works in principle with longer times, albeit with reduced visibility. Indeed, HBT famously obtained their results on the angular diameter of Sirius with a visi-

bility as low as 10^{-5}. In their case, integrating longer simply improved the SNR, and Classen *et al.* (2017) analogously suggested improving the SNR of an IDI experiment by simply summing a larger number of diffraction patterns.

2.1 The IDI Signal-to-noise Ratio

For IDI to be a viable technique, it must be possible to realize a strong signal-to-noise ratio under reasonable experimental conditions. While Classen *et al.* (2017) discussed increasing the SNR by averaging over additional patterns, they did not examine in detail the various factors affecting the SNR. Trost *et al.* (2020) rigorously examined the question of SNR in an IDI experiment for the first time. They rederived the results of Classen *et al.* (2017) for $g^{(2)}(\mathbf{q})$ in the both the SPE and TLS cases, and then assumed enough emitters exist to consider the TLS case.

Two sources of noise they distinguished were the Poisson noise (or "shot noise") that is characteristic of the quantum nature of light when integrated on a pixelated detector and the "phase noise" that occurs due to the nature of the random phases of the waves generating a finite number of speckle patterns. The latter of these was not addressed in the noise calculations by Hanbury Brown and Twiss (Brown and Twiss, 1957, 1958) in their treatment of the SNR of an intensity interferometer. Futhermore, they added the visibility factor $\mathcal{V}$ as a coefficient modulating the amplitude of $|g^{(1)}(\mathbf{q})|^2$ and identified it with the inverse of the number of modes, $\mathcal{V} = 1/M$, where photons are in the same mode M if they are temporally coherent and so exhibit interference. For unpolarized light and in the limit of long exposure times T relative to the coherence time τ_c, the number of modes is

$$M \approx 2T/\tau_c. \tag{2.5}$$

This is the limit relevant when the pulse duration is longer than the coherence time, as is

currently the case at XFELs. Other effects they identified that adversely effect the visibility are sampling limitations of the speckle pattern due to the finite solid angle of detector pixels and the energy resolution of the detector, which may not be capable of distinguishing between $K_{\alpha,1}$ and $K_{\alpha,2}$ lines. The latter degeneracy reduces the visibility to 5/9 of the full value.

After an involved discussion on the statistics of the autocorrelation function, they derived that

$$SNR = \frac{\mu^2 \sqrt{N_P}\sqrt{C(\mathbf{q})}}{M\sqrt{\frac{1+4M}{M^2}\mu^4 + 2\frac{1+2M}{M}\mu^3 + \mu^2}} \left|\frac{\tilde{S}(\mathbf{q})}{\tilde{S}(0)}\right|^2, \qquad (2.6)$$

where μ is the mean photon count per pixel, N_P is the number of exposures, and $C(\mathbf{q})$ is the multiplicity of different pixel pairs with the same vector $\mathbf{q}$ (which is high for small $\mathbf{q}$ and low for large $\mathbf{q}$). This expression is just the expected value of the autocorrelation of all photon pairs divided by the square root of its variance.

Of particular note are the two limiting behaviors of Equation (2.6) for low and high μ. The low-μ case where the Poisson noise dominates reduces to

$$SNR = \frac{\mu\sqrt{N_P}\sqrt{C(\mathbf{q})}}{M} \left|\frac{\tilde{S}(\mathbf{q})}{\tilde{S}(0)}\right|^2 \qquad (2.7)$$

while the high-μ case dominated by the phase noise yields

$$SNR = \frac{\sqrt{N_P}\sqrt{C(\mathbf{q})}}{\sqrt{1+4M}} \left|\frac{\tilde{S}(\mathbf{q})}{\tilde{S}(0)}\right|^2. \qquad (2.8)$$

The latter limit is notably independent of μ, meaning that at high photon counts the SNR plateaus to a constant value. In the lower limit the SNR scales linearly with μ.

In the case where the sample is a sufficiently large crystal, the quantity $\left|\frac{\tilde{S}(\mathbf{q})}{\tilde{S}(0)}\right|^2$ approaches a limiting behavior of $1/N_E$, where N_E is the number of emitters. This simplifies the low-μ limit to $SNR = \mu\sqrt{N_P}\sqrt{C(\mathbf{q})}/(N_E M)$. Trost *et al.* (2020) argued that this behavior makes the SNR better for smaller samples than larger ones, contrary to the behavior

expected in CDI where $SNR \propto \sqrt{N_E}$. They explained that larger crystals imply smaller speckles which then lower μ, as the pixel size or detector position must be adjusted to compensate, and also that larger crystals suffer from increased numbers of modes due to exceeding the characteristic length of $c\tau_c$. The conclusion they arrive at is that IDI, unlike CDI, fundamentally favors smaller samples despite the low number of counts per pixel because $SNR \propto 1/N_E$.

Although Trost *et al.* (2020) derived the SNR expression for IDI and concluded that the technique should be feasible, they considered a wide range of possible values of μ from 10^{-2} to 10^3 without quantifying what in this range is realistic. Lohse *et al.* (2021) presented a thorough analysis of many factors that affect the SNR in IDI and estimated a value for μ. They argued that $\mu \leq 0.1$ is actually the only realistic range, with the upper limit applying to a very dense sample of emitters such as a crystal of pure iron imaged under ideal conditions. Actual biomolecules, being considerably less dense than this, suffer from extremely low signal counts and are squarely in the Poisson-dominated limit of Equation (2.6), with the phase noise that dominates the high-μ limit having no relevance.

A natural solution to overcome this would be to increase the crystal volume, and therefore the number of emitters, but they also derived a constraint on the transverse crystal geometry (as measured relative to the beam direction) in the case of small $|\mathbf{q}|$ that

$$\mathcal{V} \leq \frac{2c\tau_c}{|\mathbf{q}|L_{trans}}. \tag{2.9}$$

That is, the maximum visibility is bounded by the coherence time and the transverse sample size L_{trans}. Futhermore, a comparable constraint also applies to the other two dimensions of the crystal when considering large values of $|\mathbf{q}|$. This was the precise form of the size constraints that Trost *et al.* (2020) had alluded to as a justification for why smaller crystals yield superior SNR. Thus, the product $\mathcal{V} \times \mu$ that appears in Equation (2.6) has an upper bound, with larger crystals increasing μ until some optimal size beyond which $\mathcal{V}$ begins to

decrease. Coupled with the very low values of μ that they already expected for biomolecules, they were pessimistic that IDI is possible at X-ray energies without requiring extraordinary numbers of patterns, possibly well above 10^7, to meet an acceptable SNR—though they were careful to point out that these issues are greatly alleviated at longer coherence times, and therefore IDI at longer wavelengths should be possible. This result does appear to be in tension with the conclusions of Trost *et al.* (2020) that IDI with sufficiently small crystals should be feasible owing to the favorable dependence on the number of emitters.

2.2   IDI Experiments at XFELs

One regime where the analysis of Lohse *et al.* (2021) *did* conclude that this type of imaging was possible at XFELs was the case of much larger geometry, particularly when only the overall geometry of the sample and beam were of interest, such as a thin sheet made of a transition metal used to characterize the spot size of the XFEL beam and its pulse duration. More general applications of intensity interferometry at XFELs have a longer history than IDI, with at least two earlier experiments being conducted at FLASH (Singer *et al.*, 2013) and at LCLS (Song *et al.*, 2014). The Vartanyants group at the DESY laboratory, in their intensity interferometry work at FLASH examining the statistical properties of the XFEL beam, foresaw two possible future applications of intensity correlations. The first was the study of seeded FELs to assess their temporal coherence and compare it with SASE-generated FELs. The second was the possibility of studying the dynamics of ultrafast processes at FELs, with the specific example of studying the Coulomb explosion of a single molecule to learn about how its size changes as a function of time. They did not mention imaging of the sample with atomic precision.

The most recent experiment of this type was completed at the SPring-8 Angstrom Com-

pact free-electron LAser (SACLA) by Inoue *et al.* (2019). In light of upcoming attosecond pulse durations at compact XFELs, they cited a need for new techniques capable of measuring the duration of XFEL pulses shorter than 10 fs and used intensity interferometry to do so. The experimenters collected data from 1047 pulses of 12 keV photons incident on a 20 μm-thick copper foil tilted at $30°$. Notably, the detector was placed just off the optical axis rather than at $90°$ as proposed by Classen *et al.* (2017). They observed clear intensity correlations with this setup as shown in Figure 5. The intensity correlations were fit well by a 2D Gaussian beam profile of transverse widths $\sigma_x = 0.4$ μm and $\sigma_y = 0.5$ μm. The duration of the XFEL pulse was computed from the visibility of the correlations assuming a Gaussian of standard deviation σ_t, and thus a full-width at half-maximum of $2\sqrt{2\ln 2}\sigma_t = 10.3$ fs. Trost *et al.* (2020) pointed out that the analysis of Inoue *et al.* (2019) failed to account for the unpolarized nature of the XFEL beam, which halved the correlation of the intensity fluctuations. The erratum Inoue *et al.* (2021) corrected for the lack of polarization with the new conclusion that the visibility was 0.0262 ± 0.008 and the pulse duration was 5.1 ± 0.2 fs—half of the result originally reported.
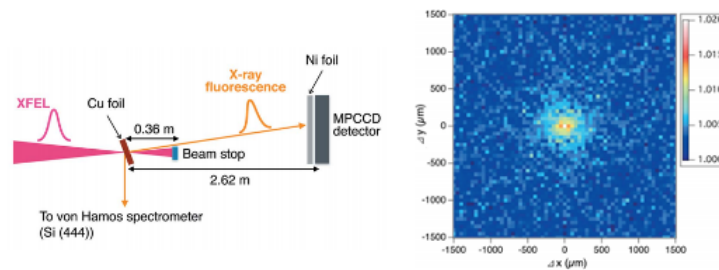

Figure 5. SACLA experiment design and results

Figure. The experiment reported by Inoue *et al.* (2019) showing a design with a fixed-target sample and a detector placed in the forward detection (left) as well as the actual intensity correlations (right).

The first experiment designed specifically with the IDI paradigm of Classen *et al.* (2017)

in mind was carried out at the MFX instrument of LCLS in April 2018 by the Chapman group of the Center for Free-electron Laser Science at DESY (Trost *et al.*, 2022). The chosen samples were irregularly-shaped iron "nanostars" approximately 100 nm in diameter, with a goal of measuring the first Bragg peak through correlations in the iron K_α fluorescence using 15 fs and 3 fs pulses. Figure 6 shows the basic experimental design with detectors simultaneously placed in the forward direction to do CDI and at 90° for the fluorescence detection. The purpose of simultaneously doing CDI with IDI was to use the CDI patterns to determine which IDI patterns correspond to sample hits and to identify the sample's orientation via standard pattern indexing procedures. The choice of 90° for detecting fluorescence was motivated by the discussion in Classen *et al.* (2017) that this direction should minimize the elastic scattering background. A large conical manganese filter was placed over the detector to absorb stray elastic scattering and Fe K_β fluorescence, but had the unintended effect of creating Mn fluorescence as additional background noise.
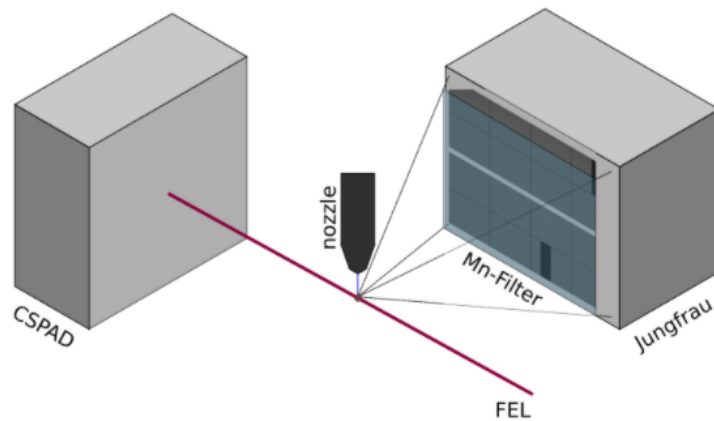

Figure 6. Schematic of the first IDI experiment

Figure. This image from Trost *et al.* (2022) demonstrates the geometry of the first IDI experiment, with the sample injected from above and the fluorescence detected perpendicular to the beam axis to minimize the contribution from elastic scattering.

Trost *et al.* (2022) report that the energy resolution of the detector was not sufficient to reliably distinguish $K_{\alpha,1}$ and $K_{\alpha,2}$ photons, lowering the overall visibility by a factor of 5/9, and that the patterns overall were very sparse, with average count rates of 9×10^{-4} photons per pixel. They predicted a maximum possible speckle contrast given by $\mathcal{V} = \frac{5(1+P^2)}{18} \frac{\tau_c}{T}$ (where P^2 is a polarization factor that vanishes when the detector is insensitive to the X-ray polarization) of $\mathcal{V} = 0.038$ for the 3 fs pulses and $\mathcal{V} = 0.0076$ for the 15 fs pulses. However, they note that these ideal values are further reduced by insufficient sampling of the speckles, background photons attributed to the manganese filter, and limitations due to the sample size and the experimental geometry. Iron K_α fluorescence has a coherence time of 0.4 fs, which yields a light-travel distance of $c\tau_c \approx 120$ nm. As the nanostars are roughly 100 nm in size, they may not be completely coherent across the whole sample.

A naive calculation of the visibility from 61,000 3 fs patterns and 98,000 15 fs patterns found unphysical results due to large variations in the mean pattern intensity $\langle I \rangle$. This necessitated a new method of determining $\mathcal{V}$ in which the estimate of $\mathcal{V}$ for each pattern was weighted by the inverse of its variance. Trost *et al.* (2022) showed that this method worked in simulations, but when applied to the data produced slightly negative visibilities, indicating sub-Poissonian statistics that were not anticipated. Their reasoning was that their photonization algorithm systematically underestimated two-photon hits relative to one-photon hits, so an absolute estimation of the visibility, and therefore detection of intensity correlations, was not possible. Instead they quoted a relative difference in the visibility of the 3 fs and 15 fs pulses of $\Delta \mathcal{V} = 0.025 \pm 0.005$, whereas the expected difference in contrast due to the change in the X-ray pulse duration should be at most $\Delta \mathcal{V} = 0.0304$. This physically meaningful result is consistent with the hypothesis that the speckle contrast *was* caused by intensity correlations due to X-ray fluorescence. However, without an absolute value for the visibility it was not possible to extract the structure factor and perform a reconstruction of the sample.

Still, this first result detecting correlations provides some evidence against the pessimism of Lohse *et al.* (2021) toward IDI for the atomic scale.

A follow-up IDI experiment that has been completed by the Chapman group and is currently undergoing analysis was performed at the MID instrument at European XFEL in November 2021. The proposal for this experiment called for imaging of a metal sheet (with sheets made of different elements between Cr and Ge) attached to a 30 μm-thick sheet of tungsten with pulse durations between 3 and 30 fs. For each sheet the tungsten would have micron-sized holes milled by a focused ion beam at select locations, creating different masks. The tungsten would filter out elastic scattering and inner-shell fluorescence of the transition metal at all points except where the holes are located, permitting only fluorescence in the shape of the mask to reach the detector. In addition to using large targets of known geometry with high emitter densities as a proof-of-concept for future atomic-scale attempts at IDI, the proposal cited that two other goals of the experiment were to explore the coherence properties of the fluorescence in the forward direction (see Chapter 3 for motivation discussing this choice) and to lower the beam intensity to less than 10^7 photons/μm^2 to limit damage to the sample.

Chapter 3

A TIME-DEPENDENT MODEL OF IDI AND ITS IMPLICATIONS

In this chapter, a time-dependent semiclassical theory of IDI and accompanying simulations are presented. Adding time-dependence has significant consequences for IDI experiments that were not identified in the static treatments of Classen *et al.* (2017) or Trost *et al.* (2020). In particular, time-dependence affects the direction in which the strongest intensity correlations are observed and reveals precisely how the duration of the XFEL pulse effects the visibility of those correlations. The consequences of these results for IDI experiments at compact XFELs are studied, with the aim of calculating the resolution and contrast of reconstructed three-dimensional images of biomolecules, such as viruses and proteins containing fluorescent heavy atoms, as a function of the ratio of the XFEL pulse duration to the lifetime of the inner-shell fluorescence. We use the Hybrid Input Output algorithm (Fienup, 1982) to address the phase problem in our simulations (see Hawkes and Spence (2007) for a review). Where applicable, the calculations are done in Heaviside-Lorentz units. The results in this chapter were published in Shevchuk *et al.* (2021).

3.1   A Semiclassical Model for IDI

Fluorescence observed in the far field is dominated by the dipole term in Maxwell's equations. The emitters in the sample can therefore be approximated by an array of N point-like, damped, dipole radiators indexed by n and each defined by a time-dependent vector

$$\mathbf{p}_n(t) = \mathbf{p}_{n_0} e^{-\Gamma(t-t_n)/2} \sin\left(\omega_0 t + \phi_n\right)\Theta(t - t_n). \tag{3.1}$$

Here $\mathbf{p}_{n_0}$ is a constant dipole-moment vector that spatially orients the emitter and the fluorescence occurs at time t_n with mean angular frequency ω_0 and initial phase ϕ_n, where the latter is defined such that it absorbs a term of the form $\omega_0 t_n$. The damping coefficient Γ is the Einstein coefficient for spontaneous emission and the inverse of the decay time of the excited state. It defines the half-width at half-maximum of a Lorentzian line profile governed purely by radiative broadening, which is assumed to be the dominant effect on the linewidth.

The complicated intra-atomic physics between photoionization and fluorescence are also assumed to occur on a timescale much shorter than the fluorescence lifetime and may be safely be ignored. Therefore, t_n in the model is also when the atom is photoionized and the step function $\Theta(t - t_n)$ ensures that emitters only contribute post-excitation. The initial parameters $\mathbf{p}_{n_0}$, t_n, and ϕ_n are treated as random variables for each value of n as discussed in Sections 3.1.1–3.1.3.

From Equation (3.1) the resulting polarization density can be defined as $\mathbf{P}_n(t) = \mathbf{p}_n(t)\delta^3(\mathbf{r} - \mathbf{r}_n)$ for the emitter with position $\mathbf{r}_n$. It contributes an electromagnetic current density

$$\mathbf{J}_n(\mathbf{r}, t) = \frac{d\mathbf{P}_n(\mathbf{r}, t)}{dt} = \omega_0 \mathbf{p}_{n_0} e^{-\Gamma(t-t_n)/2} \cos{(\omega_0 t + \phi_n)} \delta^3(\mathbf{r} - \mathbf{r}_n)\Theta(t - t_n). \qquad (3.2)$$

For inner shell X-ray fluorescence, $\omega_0 \gg \Gamma$ and all terms of order Γ/ω_0 are henceforth discarded as they arise in the calculations.

Maxwell's equations expressed in potential form, assuming the Lorenz gauge, are

$$\frac{\partial^2 \Phi(\mathbf{r}, t)}{c^2 \partial t^2} - \nabla^2 \Phi(\mathbf{r}, t) = \rho(\mathbf{r}, t), \qquad (3.3)$$

$$\frac{\partial^2 \mathbf{A}(\mathbf{r}, t)}{c^2 \partial t^2} - \nabla^2 \mathbf{A}(\mathbf{r}, t) = \frac{1}{c}\mathbf{J}(\mathbf{r}, t). \qquad (3.4)$$

Using Equation (3.2), the general solution for the retarded vector potential generated by the

nth emitter is

$$
\begin{aligned}
\mathbf{A}_n(\mathbf{r}, t) &= \frac{1}{4\pi c} \int \frac{\mathbf{J}_n(\mathbf{r}', t - |\mathbf{r} - \mathbf{r}'|/c)}{|\mathbf{r} - \mathbf{r}'|} d^3\mathbf{r}' \\
&= \frac{\omega_0 \mathbf{P}_{n_0}}{4\pi c |\mathbf{r} - \mathbf{r}_n|} e^{-\Gamma(t - t_n - |\mathbf{r} - \mathbf{r}_n|/c)/2} \cos\left(\omega_0(t - t_n - |\mathbf{r} - \mathbf{r}_n|/c) + \phi_n\right) \\
&\quad \times \Theta(t - t_n - |\mathbf{r} - \mathbf{r}_n|/c).
\end{aligned}
\tag{3.5}
$$

The sample's diameter is assumed to be much smaller than the distance to the detector and the sample is taken to be near the origin of the coordinate system. The far-field approximation then simplifies the term in the denominator to $|\mathbf{r} - \mathbf{r}_n| \approx |\mathbf{r}| = r$ and the terms in the numerator to $|\mathbf{r} - \mathbf{r}_n| \approx r - \hat{\mathbf{r}} \cdot \mathbf{r}_n$. Defining for notational clarity $T_n = t_n + c^{-1}r - c^{-1}\hat{\mathbf{r}} \cdot \mathbf{r}_n$, Equation (3.5) becomes

$$
\mathbf{A}_n(\mathbf{r}, t) = \frac{\omega_0 \mathbf{P}_{n_0}}{4\pi c r} e^{-\Gamma(t - T_n)/2} \cos\left(\omega_0(t - T_n + t_n) + \phi_n\right) \Theta(t - T_n).
\tag{3.6}
$$

From this, the vacuum form of Equation (3.4) simplifies to $\frac{\partial \mathbf{E}_n(\mathbf{r}, t)}{c \partial t} = \nabla \times (\nabla \times \mathbf{A}_n(\mathbf{r}, t))$. Substituting Equation (3.6), the electric field of the fluorescence is

$$
\mathbf{E}_n(\mathbf{r}, t) = \frac{\omega_0^2}{4\pi c^2 r}(\mathbf{p}_{n_0} - (\mathbf{p}_{n_0} \cdot \hat{\mathbf{r}})\hat{\mathbf{r}}) e^{-\Gamma(t - T_n)/2} \sin\left(\omega_0(t - T_n + t_n) + \phi_n\right) \Theta(t - T_n).
\tag{3.7}
$$

As a consistency check, the vacuum relation $\mathbf{B}_n(\mathbf{r}, t) = \hat{\mathbf{r}} \times \mathbf{E}_n(\mathbf{r}, t)$ yields the same result as $\mathbf{B}_n(\mathbf{r}, t) = \nabla \times \mathbf{A}_n(\mathbf{r}, t))$.

The total energy radiated by a single emitter located at $\mathbf{r}_n$ and fluorescing at time t_n is the integral of the Poynting vector $\mathbf{S}_n = \mathbf{E}_n \times \mathbf{B}_n$ over a closed surface S with normal vector $\hat{\mathbf{n}}$

for all $t > t_n$:

$$
\begin{aligned}
W_n &= \int_{T_n}^{\infty} \int_S c(\mathbf{E}_n(\mathbf{r}, t) \times \mathbf{B}_n(\mathbf{r}, t)) \cdot d\hat{\mathbf{n}} dt \\
&= \int_{T_n}^{\infty} \int_S c(\mathbf{E}_n(\mathbf{r}, t) \times (\hat{\mathbf{r}} \times \mathbf{E}_n(\mathbf{r}, t))) \cdot d\hat{\mathbf{n}} dt \\
&= \int_{T_n}^{\infty} \int_S |\mathbf{E}_n(\mathbf{r}, t)|^2 r^2 c d\Omega dt \\
&= \int_{T_n}^{\infty} \int_S \frac{\omega_0^4 |\mathbf{p}_{n_0}|^2}{32\pi^2 c^3} \left(\hat{\mathbf{p}}_{n_0}^2 - (\hat{\mathbf{p}}_{n_0} \cdot \hat{\mathbf{r}})^2 \right) e^{-\Gamma(t-T_n)} \Theta(t - T_n) d\Omega dt \\
&= \frac{\omega_0^4 |\mathbf{p}_{n_0}|^2}{12\pi c^3 \Gamma}.
\end{aligned}
\tag{3.8}
$$

The righthand expression on the fourth line of Equation (3.8) is the cycle-averaged intensity and the integral over the solid angle makes use of the vector identity $\int (\mathbf{a} \cdot \hat{\mathbf{p}})(\mathbf{b} \cdot \hat{\mathbf{p}}) d\Omega_{\hat{\mathbf{p}}} = 4\pi(\mathbf{a} \cdot \mathbf{b})/3$. The magnitude of the dipole moment vector is normalized to

$$
|\mathbf{p}_{n_0}| = \sqrt{\frac{12\pi\hbar c^3 \Gamma}{\omega_0^3}}
\tag{3.9}
$$

by requiring that a single photon has energy $W_\gamma = \hbar\omega_0$.

From Equation (3.8) it is clear that T_n can be interpreted as the time fluorescence from the nth emitter reaches a point on an integrating detector. The cycle-averaged intensity of an ensemble of N emitters observed at the surface of a detector in the direction $\mathbf{k} = (\frac{\omega}{c})\hat{\mathbf{r}}$ is

$$
\bar{I}(\mathbf{k}, t) = \sum_{m,n}^N \overline{\mathbf{E}_m \cdot \mathbf{E}_n} = \sum_{m,n}^N \frac{3\hbar\omega_0 \Gamma}{8\pi c r^2} \left(\hat{\mathbf{p}}_{m_0} \cdot \hat{\mathbf{p}}_{n_0} - (\hat{\mathbf{p}}_{m_0} \cdot \hat{\mathbf{k}})(\hat{\mathbf{p}}_{n_0} \cdot \hat{\mathbf{k}}) \right) e^{-\Gamma(2t - T_m - T_n)/2}
$$
$$
\times e^{i(\mathbf{k} \cdot (\mathbf{r}_m - \mathbf{r}_n) + \phi_m - \phi_n)} \Theta(t - \max(T_m, T_n)), \quad (3.10)
$$

where the normalization of Equation (3.9) has been included and a conversion to reciprocal space coordinates has been made for use at the detector. The total fluence (energy per pulse per unit area) in the $\mathbf{k}$-direction is then

$$
I(\mathbf{k}) = \int_{\infty}^{\infty} \bar{I}(\mathbf{k}, t) c dt = \sum_{m,n}^N \frac{3\hbar\omega_0}{8\pi r^2} \left(\hat{\mathbf{p}}_{m_0} \cdot \hat{\mathbf{p}}_{n_0} - (\hat{\mathbf{p}}_{m_0} \cdot \hat{\mathbf{k}})(\hat{\mathbf{p}}_{n_0} \cdot \hat{\mathbf{k}}) \right) e^{-\Gamma|T_m - T_n|/2}
$$
$$
\times e^{i(\mathbf{k} \cdot (\mathbf{r}_m - \mathbf{r}_n) + \phi_m - \phi_n)}.
\tag{3.11}
$$

This expression measures the integrated intensity at a point on the detector and captures the interference of the electric fields, which only overlap significantly if the waves arrive at the same pixel within the coherence time $\tau_c = 2/\Gamma$. As Equation (3.10) has an exponential falloff in t with a coherence time much shorter than the exposure length, integrating over all future time closely approximates a snapshot in essentially all cases. The appearance of the $|T_m - T_n|$ term occurs because the wavefronts can arrive at a point on the detector in either order, but the cross terms in m and n will not contribute to Equation (3.11) until both wavefronts have arrived at that point. The integration variable can be redefined as $t_\ell = t - \max(T_m, T_n)$, which is the time of the later arrival, and integrated from zero to infinity.

As established previously, in an intensity interferometry experiment the observable quantity is the degree of second-order coherence in the field amplitudes

$$g^{(2)}(\mathbf{q}) = \sum_{i,j} g^{(2)}(\mathbf{k}_i, \mathbf{k}_j) = \sum_{i,j} \frac{\langle I(\mathbf{k}_i) I(\mathbf{k}_j) \rangle}{\langle I(\mathbf{k}_i) \rangle \langle I(\mathbf{k}_j) \rangle}, \tag{3.12}$$

where the angle brackets represent the average over an ensemble of exposures and $\mathbf{q}$ is the set of all $\mathbf{q}_{ij} = \mathbf{k}_i - \mathbf{k}_j$ for each pair of detector pixels (i, j). In this dipole model the polarization direction, phase, and ionization/emission time are considered as the variables of the ensemble that are randomized from exposure to exposure. Importantly, the random ionization times t_n, phases ϕ_n, and dipole moments p_{n_0} for all N emitters are assumed to be uncorrelated with each other and the average product of intensities takes the form

$$\langle I(\mathbf{k}_i) I(\mathbf{k}_j) \rangle = \sum_{m,n,m',n'}^{N} \frac{9\hbar^2 \omega_0^2}{64\pi^2 r^4}$$

$$\times \left\langle \left[\hat{\mathbf{p}}_{m_0} \cdot \hat{\mathbf{p}}_{n_0} - (\hat{\mathbf{p}}_{m_0} \cdot \hat{\mathbf{k}}_i)(\hat{\mathbf{p}}_{n_0} \cdot \hat{\mathbf{k}}_i) \right] \left[\hat{\mathbf{p}}_{m'_0} \cdot \hat{\mathbf{p}}_{n'_0} - (\hat{\mathbf{p}}_{m'_0} \cdot \hat{\mathbf{k}}_j)(\hat{\mathbf{p}}_{n'_0} \cdot \hat{\mathbf{k}}_j) \right] \right\rangle_\Omega$$

$$\times \left\langle e^{-\Gamma(|T_{mi} - T_{ni}| + |T_{m'j} - T_{n'j}|)/2} \right\rangle_t \left\langle e^{i(\mathbf{k}_i \cdot (\mathbf{r}_m - \mathbf{r}_n) + \phi_m - \phi_n)} e^{-i(\mathbf{k}_j \cdot (\mathbf{r}_{m'} - \mathbf{r}_{n'}) + \phi_{m'} - \phi_{n'})} \right\rangle_\phi. \tag{3.13}$$

The bracket subscripts Ω, t, and ϕ indicate that these terms are respectively averaged over solid angle, ionization time, and phase. The quantity T_{mi} is the same shorthand expression

defined before Equation (3.6) but is now adapted to the direction of the ith pixel. Additional uncorrelated parameters can be added to the model as factors to average over in this expression, including degrees of freedom for the overall position and orientation of the ensemble of emitters, and for whether or not the emitter relaxes through the desired fluorescence channel. The fact that the orientation of the sample is assumed to be constant in each shot makes our present treatment best suited to the study of fixed targets, but it also applies to any subset of shots collected from randomly-oriented samples that have been indexed to have substantially the same orientation. The dipole moment and phase averages will be computed presently and the computation of the emission time average will be deferred to Sections 3.1.2 and 3.1.3.

3.1.1 Ensemble Averaging

The behavior of the phase factors in the average is the key to achieving nonzero intensity correlations. In computing the average intensity $\langle I(\mathbf{k}_i) \rangle$, the phase term

$$\sum_{m,n}^{N} \langle e^{i(\mathbf{k}\cdot(\mathbf{r}_m - \mathbf{r}_n) + \phi_m - \phi_n)} \rangle_\phi = \sum_{m,n}^{N} \frac{1}{4\pi^2} \int_0^{2\pi} \int_0^{2\pi} e^{i(\mathbf{k}\cdot(\mathbf{r}_m - \mathbf{r}_n) + \phi_m - \phi_n)} d\phi_m d\phi_n \qquad (3.14)$$

vanishes for all $m \neq n$ and the average intensity simplifies to

$$\langle I(\mathbf{k}_i) \rangle = \frac{3N\hbar\omega_0}{8\pi r^2} \langle \hat{\mathbf{p}}_0^2 - (\hat{\mathbf{p}}_0 \cdot \hat{\mathbf{k}}_i)^2 \rangle_\Omega = \frac{N\hbar\omega_0}{4\pi r^2} \qquad (3.15)$$

where the integral over solid angle is the normalized version of the one evaluated in Equation (3.8). However, the phase term in Equation (3.13) is

$$\sum_{m,n,m',n'}^{N} \langle e^{i(\mathbf{k}_i\cdot(\mathbf{r}_m - \mathbf{r}_n) + \phi_m - \phi_n)} e^{-i(\mathbf{k}_j\cdot(\mathbf{r}_{m'} - \mathbf{r}_{n'}) + \phi_{m'} - \phi_{n'})} \rangle_\phi$$

$$= \sum_{m,n,m',n'}^{N} \frac{1}{16\pi^4} \int_0^{2\pi} \int_0^{2\pi} \int_0^{2\pi} \int_0^{2\pi} e^{i(\mathbf{k}_i\cdot(\mathbf{r}_m - \mathbf{r}_n) - \mathbf{k}_j\cdot(\mathbf{r}_{m'} - \mathbf{r}_{n'}))}$$

$$\times e^{i(\phi_m - \phi_n - \phi_{m'} + \phi_{n'})} d\phi_m d\phi_n d\phi_{m'} d\phi_{n'} \qquad (3.16)$$

Clearly, Equation (3.16) vanishes unless the phase terms cancel and this *only* happens in three cases: $m = n = m' = n'$, $m = n$ and $m' = n'$ but $m \neq m'$, and $m = m'$ and $n = n'$ but $m \neq n$. Simplifying terms results in

$$\frac{\langle I(\mathbf{k}_i)I(\mathbf{k}_j)\rangle}{\langle I(\mathbf{k}_i)\rangle\langle I(\mathbf{k}_j)\rangle} = \sum_m^N \frac{9}{4N^2} \left\langle \left[1 - (\hat{\mathbf{p}}_{m_0} \cdot \hat{\mathbf{k}}_i)^2\right]^2 \right\rangle_\Omega$$

$$+ \sum_{m \neq m'}^N \frac{9}{4N^2} \left\langle \left[1 - (\hat{\mathbf{p}}_{m_0} \cdot \hat{\mathbf{k}}_i)^2\right] \left[1 - (\hat{\mathbf{p}}_{m_0'} \cdot \hat{\mathbf{k}}_j)^2\right] \right\rangle_\Omega$$

$$+ \sum_{m \neq n}^N \frac{9}{4N^2} \left\langle \left[\hat{\mathbf{p}}_{m_0} \cdot \hat{\mathbf{p}}_{n_0} - (\hat{\mathbf{p}}_{m_0} \cdot \hat{\mathbf{k}}_i)(\hat{\mathbf{p}}_{n_0} \cdot \hat{\mathbf{k}}_i)\right] \left[\hat{\mathbf{p}}_{m_0} \cdot \hat{\mathbf{p}}_{n_0} - (\hat{\mathbf{p}}_{m_0} \cdot \hat{\mathbf{k}}_j)(\hat{\mathbf{p}}_{n_0} \cdot \hat{\mathbf{k}}_j)\right] \right\rangle_\Omega$$

$$\times \left\langle e^{-\Gamma(|T_{mi}-T_{ni}|+|T_{mj}-T_{nj}|)/2} \right\rangle_t e^{i\mathbf{q}_{ij}\cdot(\mathbf{r}_m-\mathbf{r}_n)}. \quad (3.17)$$

Averaging the over the possible phases expresses the ergodic principle. The photon phases are taken to be constant once they are generated during a given exposure. However, they are randomized for each subsequent exposure and can be considered fixed on a timescale longer than the exposure time, but shorter than the time between exposures. The limit of an average over infinitely many exposures then yields the same result as averaging the phases over an infinitely long time.

The same argument can be made for the polarization of the emitters. After further averaging the dipole moments over angle, making use of the angular integral identity before Equation (3.9) as well as the identity

$$\int (\mathbf{a} \cdot \hat{\mathbf{p}})(\mathbf{b} \cdot \hat{\mathbf{p}})(\mathbf{c} \cdot \hat{\mathbf{p}})(\mathbf{d} \cdot \hat{\mathbf{p}})d\Omega_{\hat{\mathbf{p}}} = \frac{4\pi}{15}\left[(\mathbf{a} \cdot \mathbf{b})(\mathbf{c} \cdot \mathbf{d}) + (\mathbf{a} \cdot \mathbf{c})(\mathbf{b} \cdot \mathbf{d}) + (\mathbf{a} \cdot \mathbf{d})(\mathbf{b} \cdot \mathbf{c})\right]$$

yields

$$\frac{\langle I(\mathbf{k}_i)I(\mathbf{k}_j)\rangle}{\langle I(\mathbf{k}_i)\rangle\langle I(\mathbf{k}_j)\rangle} = \frac{9}{10N}\left(1 + \frac{1}{3}(\hat{\mathbf{k}}_i \cdot \hat{\mathbf{k}}_j)^2\right) + 1 - \frac{1}{N}$$

$$+ \sum_{m \neq n}^N \frac{1 + (\hat{\mathbf{k}}_i \cdot \hat{\mathbf{k}}_j)^2}{4N^2} \left\langle e^{-\Gamma(|T_{mi}-T_{ni}|+|T_{mj}-T_{nj}|)/2} \right\rangle_t e^{i\mathbf{q}_{ij}\cdot(\mathbf{r}_m-\mathbf{r}_n)}. \quad (3.18)$$

Finally, the last term can be written as a double sum with the $m = n$ contribution subtracted off. Simplifying, this becomes

$$\frac{\langle I(\mathbf{k}_i)I(\mathbf{k}_j)\rangle}{\langle I(\mathbf{k}_i)\rangle\langle I(\mathbf{k}_j)\rangle} = 1 - \frac{7}{20N}\left(1 - \frac{1}{7}(\hat{\mathbf{k}}_i \cdot \hat{\mathbf{k}}_j)^2\right)$$
$$+ \sum_{m,n}^{N} \frac{1 + (\hat{\mathbf{k}}_i \cdot \hat{\mathbf{k}}_j)^2}{4N^2} \left\langle e^{-\Gamma(|T_{mi}-T_{ni}|+|T_{mj}-T_{nj}|)/2}\right\rangle_t e^{i\mathbf{q}_{ij}\cdot(\mathbf{r}_m-\mathbf{r}_n)}. \quad (3.19)$$

The last two terms of Equation (3.19) comprise the normalized correlation of the intensity fluctuations at two pixels on the detector, $\langle \Delta I(\mathbf{k}_i)\Delta I(\mathbf{k}_j)\rangle / \langle I(\mathbf{k}_i)\rangle\langle I(\mathbf{k}_j)\rangle$, which in a traditional HBT experiment contains information about the geometry of the source. To the extent that the term averaging over the ionization times is effectively independent of the emitter positions (which will be analyzed in Section 3.1.2), one observes that the double sum factors to $|\sum_m^N e^{i\mathbf{q}\cdot\mathbf{r}_m}|^2 = |\tilde{S}(\mathbf{q})|^2$. From $|\tilde{S}(\mathbf{q})|^2$, the real-space charge density can be reconstructed after solving the phase problem. This may be done using iterative methods to obtain the complex structure factors (Fienup, 1982). However, as described previously, the vectors $\mathbf{q}_{ij}$ have a different interpretation from conventional diffraction experiments such as CDI or small-angle X-ray scattering—they are defined here for every pair of pixels and not relative to the incident direction of the radiation as they are in the case of Bragg scattering. Each shot spans a set $\mathbf{q}$ of vectors $\mathbf{q}_{ij}$ that fill in a volume rather than just an Ewald sphere, and the largest $|\mathbf{q}_{ij}|$ extends to higher resolution than a typical coherent diffraction pattern. In the special case of only two emitters, $|\tilde{S}(\mathbf{q})|^2$ simplifies to $2 + 2\cos(\mathbf{q}\cdot(\mathbf{r}_2 - \mathbf{r}_1)) = 4\cos^2(\mathbf{q}\cdot(\mathbf{r}_2 - \mathbf{r}_1)/2)$ and the brief interference has the form of the Young's fringes generated by two coherent point sources.

The results are similar to the simplified quantum formulation of Classen *et al.* (2017) for single photon emitters in that they recover a unit term, a term $\mathcal{O}(1/N)$ to be subtracted, and a term dependent on $\mathbf{q}$. However, Equation (3.19) includes the contribution of the $m = n = m' = n'$ term that is absent in their expression. Physically, this term de-

scribes the contribution of two photons from the same atom to the pair correlation and should be excluded when considering data generated by single photon emitters. Subtracting off the contribution of this term in the model would modify the second term in Equation (3.19) to be $-\frac{5}{4N}(1 + \frac{1}{5}(\hat{\mathbf{k}}_i \cdot \hat{\mathbf{k}}_j)^2)$. The intensities in this semiclassical formalism are generated by spherical wave packets and therefore each emitter effectively contributes signal to every pixel, as though it were simultaneously emitting many identical photons. As such, the $m = n = m' = n'$ term contributes in our model and in the simulations of Section 3.2 based on it, but not to the photon correlations measured in an IDI experiment based on inner-shell fluorescence generated by an XFEL pulse.

3.1.2 Experimental Geometries for IDI

Now the focus shifts to computing the average over the initial ionization/emission times in the last term of Equation (3.19),

$$\mathcal{V} = \left\langle e^{-\Gamma(|T_{mi}-T_{ni}|+|T_{mj}-T_{nj}|)/2} \right\rangle_{t_m,t_n}. \tag{3.20}$$

The terms in the exponent of Equation (3.20) are the time differences for the wavefronts emitted at times t_m and t_n from emitters located at $\mathbf{r}_m$ and $\mathbf{r}_n$ to respectively reach pixels i and j. Effectively $\mathcal{V}$ contains all the information about the temporal coherence of the fluorescence, whereas the $e^{i\mathbf{q}_{ij}\cdot(\mathbf{r}_m-\mathbf{r}_n)}$ term it multiplies contains information about the spatial coherence of the fluorescence across the detector.

$\mathcal{V}$ is a figure of merit for an IDI experiment, so the remainder of Section 3.1 is devoted to studying how to maximize it. This will provide insight on how to optimize the design of future experiments.

The "ideal" case of a planewave pulse that instantaneously ionizes an atom as it sweeps across the sample will be examined first. The time difference between two emissions for such

a pulse is just the projection of the atomic separation along the beam direction (taken to be the z-axis): $t_m - t_n = \hat{\mathbf{z}} \cdot (\mathbf{r}_m - \mathbf{r}_n)/c$. Then the "ideal" visibility simplifies to

$$\mathcal{V} = e^{-\Gamma(|\mathbf{q}_i \cdot (\mathbf{r}_m - \mathbf{r}_n)| + |\mathbf{q}_j \cdot (\mathbf{r}_m - \mathbf{r}_n)|)/(2\omega_0)} \tag{3.21}$$

where $\mathbf{q}_i = \omega_0(\hat{\mathbf{k}}_i - \hat{\mathbf{z}})/c$ has been defined. The reader should note the vectors $\mathbf{q}_i$ are precisely those familiar from elastic scattering that are fixed to be on the Ewald sphere. The relation between the IDI vectors $\mathbf{q}_{ij}$ and the elastic scattering vectors $\mathbf{q}_i$ is $\mathbf{q}_{ij} = \mathbf{q}_i - \mathbf{q}_j$.

Two important and experimentally useful limiting cases that maximize Equation (3.21) can now be identified:

1. Choose a small sample so that $\mathbf{r}_m - \mathbf{r}_n \to 0$.

2. Place detectors toward the forward direction so that $\mathbf{q}_i, \mathbf{q}_j \to 0$.

While the first criterion is somewhat obvious and includes many interesting samples (since $c\tau_c$ for the fluorescence is optimally of order 100 nm), only by placing the detector in the forward direction can $\mathcal{V}$ generally be maximized and the correlation between the fluorescence emitted at separations much greater than $c\tau_c$ be observed. This result is nontrivial and indicates that while the fluorescence itself is isotropic, the intensity correlation in the fluorescence is not. Instead, it is strongest in the same direction as the elastic scattering. This result was not appreciated by either Classen *et al.* (2017) or Trost *et al.* (2020), where measurement of the fluorescence at $90°$ was advocated.

Figure 7 demonstrates visually and how the magnitude of the path length difference varies under these ideal pulse conditions for a few simple geometries. Due to the exponential dependence in Equation (3.21), small changes in the relative path length $c\tau$ due to adjustments in the geometry produce a large change in the visibility when the path differences are comparable to the coherence length of the fluorescence. Detecting fluorescence in the direction along the beam has a clear advantage. In effect, forward-directed fluorescence is chas-
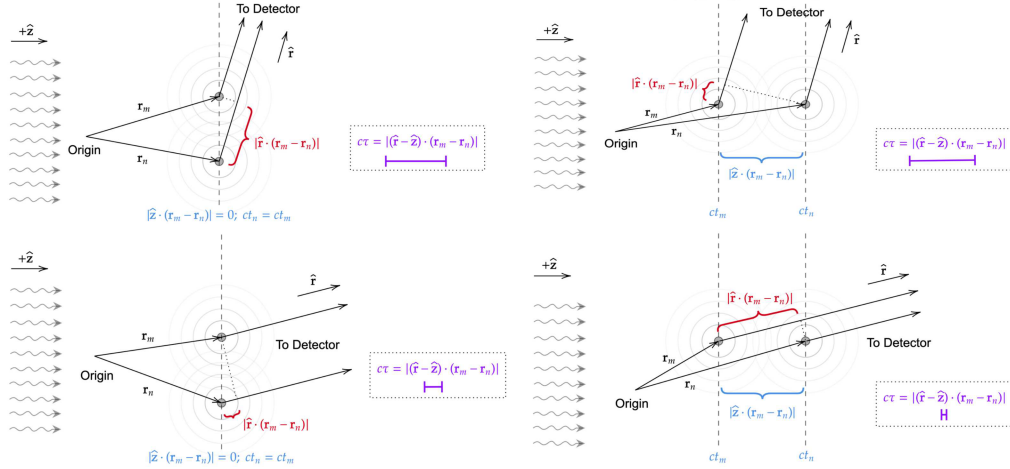
Figure 7. Sample orientations and detector positions for IDI experiments

Four different experimental geometries for IDI are shown for a pair of fluorescence emitters, as are the respective path length differences $c\tau$ (shown by the length of the purple bar) that a photon pair is delayed when arriving at one of the pixels on a detector in the far field. This length is the magnitude of the difference in the lengths of the blue and red quantities. In each case the X-ray pulse is taken to originate from the left and be instantaneously ionizing. Notice the distinction in $c\tau$ between the detectors placed way off-axis (top) and those placed slightly off-axis (bottom). Because of the exponential dependence of the visibility on $c\tau$, even a small change in this quantity due to a variation of the geometry can produce a dramatic change in the visibility when it is comparable to the coherence length of the fluorescence. Detecting fluorescence in the direction along the beam has a clear advantage over detecting it transverse to the beam.

ing the X-ray pulse as it sweeps through the sample, and so will easily interfere with other forward-directed fluorescence produced at earlier and later times. This makes the coherent volume of the sample very large. Consequently, an IDI experiment at an XFEL looking to image samples larger than the coherence length of the fluorescence should cover as large a

35

solid angle as possible in the forward direction and must be able to distinguish or otherwise filter the elastic scattering. Since the elastic scattering itself is useful for determining which shots are hits and for indexing patterns to find the sample orientation, a geometry in which the fluorescence is detected separately at a low angle off the beam axis is most practical with current detectors.

Furthermore, it is crucially seen that $\mathcal{V}$ is not independent of the emitter positions, so it cannot be simply factored out of the double sum over emitters to isolate the square of the structure factor and reconstruct the sample geometry. However, it was already established that Γ/ω_0 is quite small for the lines of interest, and if experiments implement one of the above criteria to maximize the visibility, $\mathcal{V} \approx 1$ to zeroth order.

3.1.3   IDI at a Compact XFEL

The above analysis showed how to optimize the IDI experimental geometry assuming an ideal planewave X-ray pulse where ionization occurs instantaneously. In practice, X-ray pulses have a finite duration with some probability to ionize atoms over the length of the pulse. This also affects the visibility. In this section it will be shown that $\mathcal{V}$ as derived in Equation (3.21) is supplemented by an additional factor accounting for the pulse envelope.

Assume for simplicity a monochromatic, plane-wave X-ray pulse with a time-dependent intensity $I_0(t)$ (in photons per unit area per unit time) is incident on a sample. The photoionization rate of an atom in the sample,

$$\Gamma_0(t) = I_0(t)\sigma, \tag{3.22}$$

is determined by the pulse intensity and the atomic photoionization cross-section σ at the energy of the X-ray photons. The atoms are considered to be ionized at most once over the duration of the X-ray pulse. The probability $P_n(t + \Delta t)$ that the pulse has ionized the nth

atom by a time $t + \Delta t$ for some small interval Δt is

$$P_n(t + \Delta t) = P_n(t) + (1 - P_n(t))\Gamma_0(t)\Delta t. \tag{3.23}$$

The first term is the the probability that the nth atom has been ionized by time t and the second term is the probability that it has not been ionized by time t, but is ionized in the small subsequent interval Δt with ionization probability density given by the rate $\Gamma_0(t)$. Rearranging to form a difference quotient and taking the limit as $\Delta t \to 0$ yields a differential equation for the ionization probability:

$$\frac{dP_n(t)}{dt} = \Gamma_0(t)(1 - P_n(t)). \tag{3.24}$$

$P_n(t)$ is interpretable as the cumulative distribution function of possible ionization times for the nth atom. Its general solution is

$$P_n(t) = 1 - e^{\int_0^t \Gamma_0(t')dt'}. \tag{3.25}$$

In the simple case of a rectangular X-ray pulse of length T and constant intensity $I_0(t) = I_0$, this means $P_n(t) = 1 - e^{-\Gamma_0 t}$. The ionization time of the nth emitter is given by $t_n = t_0 + t$ where t_0 is the time the pulse reaches the nth atom and $t_n < T$. While an atom will fluoresce some time after t_n, the timescale that the ion lives in an excited state is negligible and t_n is also the time at which the nth atom emits a photon. This simplification directly links the temporal coherence of the fluorescence to the properties of the XFEL beam.

Considering a plane-wave pulse of constant intensity I_0 and duration T, it is possible to show that the average over t_m and t_n yields

$$\mathcal{V} = \left(\frac{U(1 - e^{-(U+V)})}{(U + V)(1 - e^{-U})}\right)^2 e^{-\Gamma(|\mathbf{q}_i \cdot (\mathbf{r}_m - \mathbf{r}_n)| + |\mathbf{q}_j \cdot (\mathbf{r}_m - \mathbf{r}_n)|)/(2\omega_0)}. \tag{3.26}$$

Here $U = \Gamma_0 T$ and $V = \Gamma T$ are two dimensionless parameters relating the characteristic timescales in the system. The interpretation of U is that it is the average number of photons

absorbed per emitter per pulse (under the assumption that the emitter could continually absorb X-rays without exhausting its inner-shell electrons). From this model the overall amplitude of the expected visibility in an IDI experiment can be directly estimated. As described in the previous section, if the sample is substantially smaller than $c\tau_c$ or the detector is placed in the forward direction, the geometric factor (the exponential part) in Equation (3.26) is close to unity. Then the magnitude of the visibility is controlled purely by the values of U and V.

For clarity, Figure 8 plots the U and V-dependence in Equation (3.26). The key relationship is that even a reduction of many orders of magnitude in pulse intensity over that available at current XFELs (the limit of small U) has very little adverse impact on the visibility so long as the pulse duration is of order the coherence time or briefer (i.e., V is of order unity or less). To put it another way, a signal of many weakly-correlated photons can be traded for one with far fewer strongly-correlated photons to achieve the same visibility.
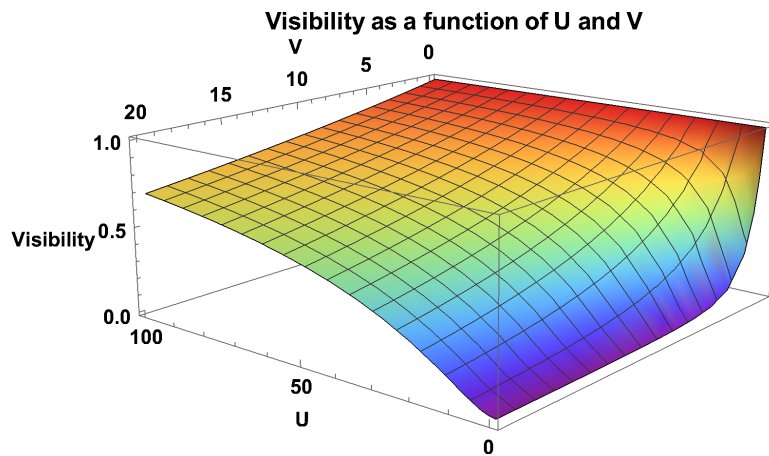

Figure 8. Visibility as a function of the parameters U and V

The prefactor of the visibility for a rectangular plane-wave pulse is plotted as a function of the ratio of the XFEL pulse duration to the lifetime of the atomic inner-shell emission (labeled V) and the ratio of XFEL pulse duration to the inverse ionization rate (labeled U). For small U, the visibility remains high so long as $V \leq 1$. In other words, short pulses produce strong correlations even if they are at low intensity. All axes are dimensionless.

Since sub-femtosecond pulses are planned for compact XFELs (Nanni *et al.*, 2018), these

machines should be ideal for IDI of heavy atoms provided that pulse fluences averaging roughly one photon per photoabsorption cross section can be achieved (that is, $U = 1$). With fluences lower than this, a significant number of atoms will not fluoresce, which will reduce the visibility by a factor proportional to the square of the probability of fluorescent emission. The flux from the CXFEL can be estimated by assuming a peak current of 500 A for 500 attoseconds at an electron beam energy of 50 MeV to yield a total stored energy of 12.5 μJ. The FEL process is approximately 0.1% efficient, yielding a coherent X-ray output of 12.5 nJ or 10^7 7 keV photons per shot. As an example, Mn has a K-edge (6.54 keV) photoabsorption cross section of $\sigma = 4.1 \times 10^{-12} \mu m^2$, which would require a focus area of approximately $4.1 \times 10^{-5} \mu m^2$ (a diameter of roughly 8 nm). A beam focus this narrow can be achieved by using a set of multilayer Laue lenses, as described recently by Bajt *et al.* (2018). Fluences that achieve $U > 1$ increase the likelihood that at least one K-shell ionization occurs, but realistically only one useful photon per emitter for IDI is expected. Therefore, there is a "sweet spot" for an IDI experiment at a compact XFEL that achieves $U \geq 1$ and $V \leq 1$. At a larger machine like LCLS or EuXFEL, $V \leq 1$ is unlikely to be achievable and such experiments will need to compensate with $U >> 1$.

A natural extension of this model is to consider a series of short rectangular pulses with a fixed spacing. In principle, a series of N_p pulses of duration T each separated by a time T_s would add both intrapulse and interpulse correlations. The latter could be possible if the pulses are sufficiently close together so that T_s is not much larger than τ_c. Pulse trains are currently in use at the European XFEL, although the spacing of the pulses there, 222 ns, is too large to be useful for IDI. At CXFEL, where sub-femtosecond pulse durations are planned, such a pulse structure should be feasible (Graves *et al.*, 2019). The machine is based on the inverse Compton effect, and uses a form of electron beam patterning to define the time structure of the X-ray pulses. Electron diffraction at a membrane imposes a spatial

pattern across the beam which becomes its time structure after passing through an emittance exchange device. In this way, the time structure may be customized, and temporal coherence retained between groups of pulses.

In the context of the SNR analysis of Trost *et al.* (2020), the lower intensity at a compact XFEL is less likely to hit the "phase noise" limit of high photon counts than a larger XFEL would, but the constraints of Lohse *et al.* (2021) suggest that this limit is only reachable for unrealistic emitter densities. Assuming IDI experiments are then Poisson-dominated, Equation (2.7) indicates that the product $V \times \mu$ should be maximized to place an upper bound on the SNR. While the same visibility V can be achieved at both compact and large XFELs, the photon count rate μ depends exclusively on the parameter U. In fact, it is directly proportional to the ionization probability, which for a pulse of length T is $P_n(t) = 1 - e^{-\Gamma_0 T} = 1 - e^{-U}$. Multiplying the prefactor in Equation (3.26) by this term provides an expression maximizing the upper bound discussed by Lohse *et al.* (2021):

$$SNR \leq \left(\frac{U^2(1 - e^{-(U+V)})^2}{(U + V)^2(1 - e^{-U})} \right). \tag{3.27}$$

This function is plotted in Figure 9 and looks similar to Figure 8 except for the strong difference in behavior at small U and V. Naturally the SNR should be zero if $U = 0$ regardless of V as no photons are ionized and no signal is produced. However, a value of $U = 1$ corresponds to a 63% probability of ionizing an emitter, so even at values of $U >> 1$, the photon count cannot even be doubled above that produced at $U = 1$ for any pulse duration. The conclusion is that there is little possible advantage to making $U >> 1$ unless $V > 1$, and at $V < 1$ merely having $U > 1$ suffices to provide the best possible SNR. Therefore, the beam properties of a compact XFEL are ideal for achieving the best possible signal-to-noise ratio for IDI.

Throughout this section the fact that the fluorescence yield is not unity for typical emitters has been ignored in favor of the simplifying assumption that ionization events translate

directly to detectable photons. However, the yield is independent of both the ionization rate and the fluorescence lifetime, so it should not modify the relative behavior of the signal-to-noise ratio as a function of U and V, and so should not affect this conclusion.
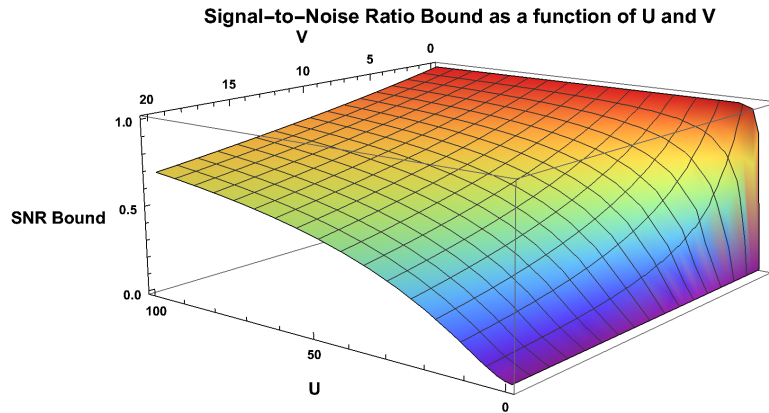

Figure 9. Signal-to-noise ratio upper bound as a function of parameters U and V

The signal-to-noise ratio upper bound for IDI with a rectangular plane-wave pulse is plotted as a function of the ratio of the XFEL pulse duration to the lifetime of the atomic inner-shell emission (labeled V) and the ratio of XFEL pulse duration to the inverse ionization rate (labeled U). For U approaching zero, the SNR vanishes regardless of V. However, only $U > 1$ is necessary to reach optimal signal-to-noise when $V < 1$. That is, among XFEL beams, compact XFELs provide the best possible SNR. All axes are dimensionless.

3.2 Simulations

For simulations based on the above model, an ensemble of fluorescing zinc atoms at fixed positions was defined, assuming at most one excitation per atom. Diffraction patterns were generated by sampling random phases, dipole moments, ionization times, and assuming an ionization rate fixed by the elemental photoabsorption cross-section and beam intensity us-

ing the model of Section 3.1.3. The random phases were sampled from a uniform distribution while the dipole moment components were sampled from three Gaussian normal distributions and the ionization times were sampled from the cumulative distribution in Equation (3.25). The latter were discarded if they extended beyond the time the X-ray pulse interacted with the sample. The incident energy (used for the ionization cross section) was 9.65 keV, the energy of the zinc K-edge, and the fluorescence had energy 8.5 keV, the zinc K_α line. For the compact XFEL simulation a 500 attosecond pulse duration was targeted and the pulse intensity was adjusted to be 2.1×10^{12} photons/fs/μm^2, which yielded a value of $U = 3$ for the zinc K-shell. For LCLS a pulse duration of 3 fs and a pulse intensity of 8.5×10^{11} photons/fs/μm^2 were assumed. This is optimistic for the current machine parameters at LCLS absent additional optics, but could be achieved with focusing from multilayer Laue lenses. These two sets of parameters were chosen so that they yield roughly the same visibility on both machines.

A spherical detector of 48-by-48 pixels was defined where polar and azimuthal directions on the sphere were partitioned into an equal number of pixels. The solid angle subtended by the pixels determined the separation resolvable from interference fringes across the detector. Since $g^{(2)}(\mathbf{q})$ does not explicitly depend on the detector distance in the far-field approximation, the simulations left it arbitrary and fixed the pixel solid angle instead of the pixel size. With a spherical detector each snapshot captured the largest possible amount of $\mathbf{q}$-space data to be used for a reconstruction.

Using Equation (3.11) and a specification of the emitter positions, the intensity at values located in the center of each pixel on the spherical detector was computed and Poisson noise was added to these values. Then $g^{(2)}(\mathbf{q})$ was computed by generating and summing 10,000 such interference patterns. In the limit of many patterns, this process is the equivalent of averaging over all possible dipole moments, ionization times, and relative phases. After com-

puting the degree of coherence, all **q**-vectors for every pixel pair were binned into voxels in **q**-space. Finally, the Hybrid Input Output phase retrieval algorithm was implemented with a feedback parameter of 0.7 to solve the phase problem and generate a reconstruction.

In Figures 10 and 11, a 12-atom icosahedral "virus capsid" of zinc emitters has been reconstructed from the simulated low-resolution IDI interference patterns with the mentioned parameters. The oversampling ratio is roughly a factor of two. As noted above, the aim is to show that similar fidelity can be achieved for the different experimental capabilities of a traditional large XFEL and a compact XFEL. While these simulations were done on a laptop computer as a proof of concept and are rather artificial, full-scale IDI simulations of this model could be done in a dedicated high-performance cluster.
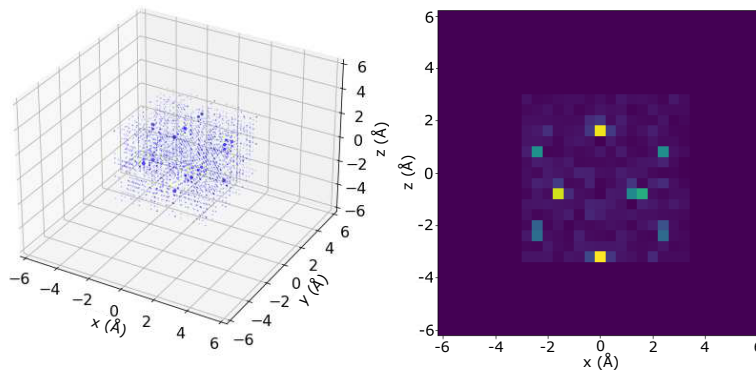

Figure 10. 3D reconstruction and 2D projection of a virus capsid

A sample reconstruction of a "virus capsid" of zinc atoms in 3D is shown (left) and projected into the $x - z$ plane (right). The simulation generated and averaged 10,000 patterns to compute the degree of coherence assuming emitters from the zinc K shell and instant ionization. Snapshots are simulated as interference patterns on a spherical detector of size 48x48 pixels and averaged to compute $g^{(2)}(\mathbf{q})$. The **q** vectors fill a spherical region in **q**-space (not shown). A flat detector also provides some 3D **q**-space data, despite spanning a plane in real space, because the **k**-vectors to each pixel have constant magnitude while their differences are not restricted to a surface. A cubic support constraint was used for the phasing.
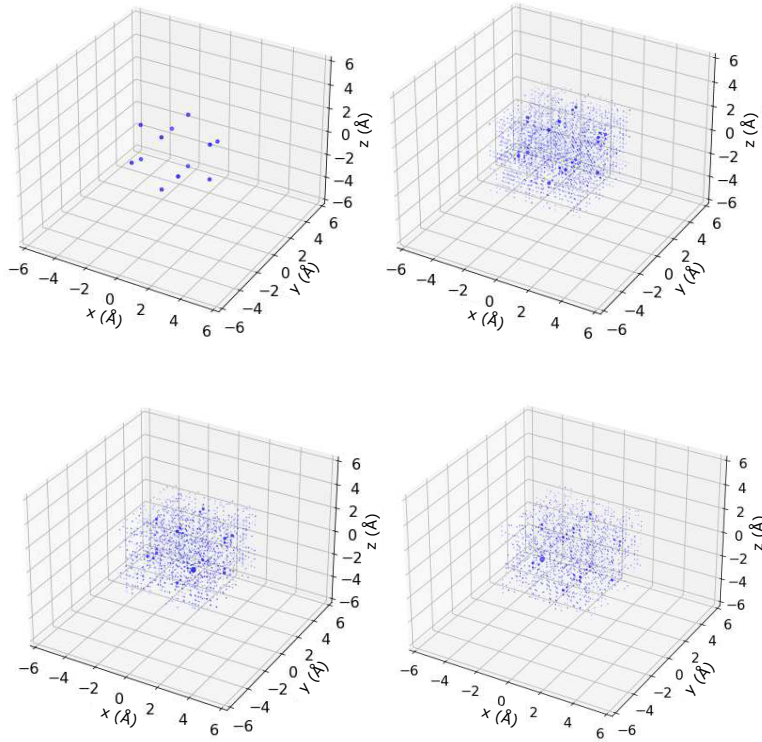
Figure 11. Capsid reconstructions for different XFEL beam parameters

Three reconstructions and a reference image of a 12-atom icosahedral zinc virus capsid are shown for different experimental IDI parameters. Clockwise from the top left are the reference structure, a reconstruction assuming the ionization occurs instantaneously, an example reconstruction with CXFEL parameters, and an example reconstruction with LCLS parameters. The pulse durations used for LCLS and CXFEL were 3 fs and 500 attoseconds respectively. For instant ionization the pulse is a Dirac δ-function, and as expected produces the best reconstruction. The two bottom panels show that similar visibility can be achieved for a reconstruction at either large XFELs or compact XFELs, subject to making the pulse duration as short as possible and focusing the beam with multilayer Laue lenses to achieve higher incident intensities on the sample.

3.3 Discussion

As is seen from Equation (3.21) and Figure 7, the potential to measure correlations over a large distance increases substantially when the detector is placed in the forward direction and this was not appreciated until the SACLA experiment described by Inoue *et al.* (2019).

This is particularly important if the coherence length of the radiation is shorter than ideal due to additional line broadening. Lohse *et al.* (2021) also recovered this result because their analysis includes time-dependence, although it was completed independently of the author's work presented here.

Although the derivation of Equation (3.26) was done using a semiclassical model, there is no reason to expect that a full treatment using quantum electrodynamics would qualitatively change the limiting behavior of the visibility for low-intensity, short-duration pulses that is critical to the success of IDI at a compact XFEL. Comparing these results to the simple quantum description given by Classen *et al.* (2017) of single photon emitters shows the same general behavior as their results, but in their model they do not calculate the effects of intensity, pulse duration, and experimental geometry on the visibility of the correlations.

The use of photoelectrons for IDI should also be possible, with the advantages of a direct interaction without "afterglow" and a strong signal, but requiring much more complex, angle-resolved, time-of-flight photoemission spectroscopy (ARPES) instrumentation. For photoelectrons the coherence time is inversely proportional to the bandwidth of the exciting XFEL beam, since the radiative decay time is negligible for very narrow inner-shell bands from which these photoelectrons originate. The relatively short inelastic mean free path of photoelectrons would restrict the method to smaller molecules, and multiple scattering of the photoelectrons may also limit the sample size. Alternatively, multiple photoelectron scattering events could provide additional structural information not present in the photon case. One clear advantage photoelectron IDI would have over X-ray fluorescence is that detection of lighter elements is possible because the signal is not limited by their low fluorescence yield. To weigh the various pros and cons, an extensive analysis of the feasibility of IDI using photoelectrons instead of X-ray fluorescence should be carried out.

3.4 Conclusion

This dissertation has presented and analyzed incoherent diffractive imaging, a new technique for atomic-scale imaging at X-ray free-electron lasers using the principles of intensity interferometry. The author has reviewed the few papers to date that have addressed this method and created a time-dependent, semiclassical framework to study the viability of IDI for structural biology at compact X-ray free-electron lasers—the upcoming generation of XFELs that are currently under construction. The primary result finds that, although the lower intensity of a compact XFEL presents limitations for traditional coherent diffractive imaging, this need not be an obstacle to the visibility or the signal-to-noise ratio in IDI as long as the pulse duration is comparable to or less than the fluorescence coherence time, the pulse can be focused with Laue lenses to a photon density that will ionize the emitters with a high probability, and the fluorescence is captured primarily in the forward direction where the radiation's temporal coherence is strongest. All of these conditions should be possible to meet at a compact XFEL, which, in fact, provides the best possible beam properties for this technique.

Despite these results, there are still concerns about the signal-to-noise ratio that can be realistically achieved in an IDI experiment. Classen *et al.* (2017) operated under the assumption that on average a detection rate of roughly five photons per pixel per exposure was reasonable, and the follow-up study by Trost *et al.* (2020) examining the SNR for a wide range of rates from 10^{-2} to 10^3 photons per pixel concluded that—unlike for CDI—the SNR for IDI experiments should favor smaller samples. The analysis of Lohse *et al.* (2021) cast significant doubt on these results, finding that they strongly overestimate the average number of photons per pixel and that the low density of transition-metal emitters in biomolecules limits the photon statistics to less than 0.1 counts per pixel even in the most idealized cases.

Moreover, this limitation cannot be overcome by simply increasing the sample size as the sample dimensions are generally constrained to be of order $c\tau_c$ lest the visibility be reduced. The upshot of their analysis is that achieving even a modest SNR for IDI may require an unreasonably large number of patterns for diffuse samples.

On the other hand, the experimental results by Inoue *et al.* (2019) demonstrate that intensity interferometry at XFELs can unambiguously resolve larger features like the focal spot size. Also, the first experiment designed specifically with IDI in mind by Trost *et al.* (2022) did show evidence that intensity correlations from X-ray fluorescence were observed despite very low photon count rates averaging less that 10^{-3} counts per pixel, but additional experiments are necessary to refine the method to a point where a reconstruction might be achieved. Whether the sample-intrinsic limitations presented by Lohse *et al.* (2021) will dampen further efforts remains to be seen, but the results presented in this dissertation strongly support the claim that compact XFELs present the best opportunity to realize IDI.

REFERENCES

Bajt, S., M. Prasciolu, H. Fleckenstein, M. Domaracký, H. Chapman, A. Morgan, O. Yefanov, M. Messerschmidt, Y. Du, K. Murray, V. Mariani, M. Kuhn, S. Aplin, K. Pande, P. Villanueva-Perez, K. Stachnik, J. Chen, A. Andrejczuk, A. Meents and C. Hamm, "X-ray focusing with efficient high-na multilayer laue lenses", Light: Science & Applications 7, 17162 (2018).

Berman, H. M., J. Westbrook, Z. Feng, G. Gilliland, T. N. Bhat, H. Weissig, I. N. Shindyalov and P. E. Bourne, "The protein data bank", Nucleic acids research 28, 1, 235–242 (2000).

Brown, R. H. and R. Twiss, "Interferometry of the intensity fluctuations in light. ii. an experimental test of the theory for partially coherent light", Proceedings of the Royal Society of London. Series A. Mathematical and Physical Sciences 243, 1234, 291–319 (1958).

Brown, R. H. and R. Q. Twiss, "Lxxiv. a new type of interferometer for use in radio astronomy", The London, Edinburgh, and Dublin Philosophical Magazine and Journal of Science 45, 366, 663–682 (1954).

Brown, R. H. and R. Q. Twiss, "Correlation between photons in two coherent beams of light", Nature 177, 4497, 27–29 (1956).

Brown, R. H. and R. Q. Twiss, "Interferometry of the intensity fluctuations in light. i. basic theory: the correlation between photons in coherent beams of radiation", Proceedings of the Royal Society of London. Series A. Mathematical and Physical Sciences 242, 1230, 300–324 (1957).

Campbell, J. and T. Papp, "Widths of the atomic k–n7 levels", Atomic Data and Nuclear Data Tables 77, 1, 1–56 (2001).

Classen, A., K. Ayyer, H. N. Chapman, R. Röhlsberger and J. von Zanthier, "Incoherent diffractive imaging via intensity correlations of hard x-rays", Phys. Rev. Lett. 119, 053401, URL https://link.aps.org/doi/10.1103/PhysRevLett.119.053401 (2017).

Fienup, J. R., "Phase retrieval algorithms: a comparison", Appl. Opt. 21, 15, 2758–2769, URL http://ao.osa.org/abstract.cfm?URI=ao-21-15-2758 (1982).

Gaffney, K. and H. N. Chapman, "Imaging atomic structure and dynamics with ultrafast x-ray scattering", science 316, 5830, 1444–1448 (2007).

Goodman, P., W. Langer and S. Brumby, "The twiss-hanbury brown controversy: a 40-years perspective", (1997).

Graves, W., S. Chang, D. Dwyer, P. Fromme, M. Holl, B. Levin, L. Malin, J. Vincent, J. Spence, E. Nanni *et al.*, "Nanopatterned electron beams for temporal coherence and deterministic phase control of x-ray free-electron lasers", arXiv preprint arXiv:1906.01525 (2019).

Graves, W., J. Chen, P. Fromme, M. Holl, R. Kirian, L. Malin, K. Schmidt, J. Spence, M. Underhill, U. Weierstall *et al.*, "Asu compact xfel", in "38th Int. Free Electron Laser Conf", (2017).

Hawkes, P. W. and J. C. Spence, *Science of microscopy*, vol. 1 (Springer, 2007).

Inoue, I., K. Tamasaku, T. Osaka, Y. Inubushi and M. Yabashi, "Determination of X-ray pulse duration via intensity correlation measurements of X-ray fluorescence", Journal of Synchrotron Radiation 26, 6, 2050–2054, URL https://doi.org/10.1107/S1600577519011202 (2019).

Inoue, I., K. Tamasaku, T. Osaka, Y. Inubushi and M. Yabashi, "Determination of x-ray pulse duration via intensity correlation measurement of x-ray fluorescence. erratum", Journal of Synchrotron Radiation 28, 1, 372–372 (2021).

Lohse, L. M., M. Vassholz and T. Salditt, "On incoherent diffractive imaging", Acta Crystallographica Section A: Foundations and Advances 77, 5 (2021).

Loudon, R., *The quantum theory of light*, Oxford science publications (Clarendon Press, 1973), URL https://books.google.com/books?id=OHspAQAAMAAJ.

Nanni, E. A., W. S. Graves and D. E. Moncton, "Nanomodulated electron beams via electron diffraction and emittance exchange for coherent x-ray generation", Phys. Rev. Accel. Beams 21, 014401, URL https://link.aps.org/doi/10.1103/PhysRevAccelBeams.21.014401 (2018).

Neutze, R., R. Wouts, D. Van der Spoel, E. Weckert and J. Hajdu, "Potential for biomolecular imaging with femtosecond x-ray pulses", Nature 406, 6797, 752–757 (2000).

Shevchuk, A. S., J. C. Spence, R. A. Kirian, W. S. Graves and K. E. Schmidt, "Imaging by intensity interferometry of x-ray fluorescence at a compact x-ray free-electron laser", Phys-

ical Review A 104, 2, 023514 (2021).

Singer, A., U. Lorenz, F. Sorgenfrei, N. Gerasimova, J. Gulden, O. Yefanov, R. Kurta, A. Sha-
balin, R. Dronyak, R. Treusch *et al.*, "Hanbury brown–twiss interferometry at a free-
electron laser", Physical review letters 111, 3, 034802 (2013).

Solem, J. C., "Imaging biological specimens with high-intensity soft x-rays", JOSA B 3, 11,
1551–1565 (1986).

Song, S., D. Zhu, A. Singer, J. Wu, M. Sikorski, M. Chollet, H. Lemke, R. Alonso-Mori, J. M.
Glownia, J. Krzywinski *et al.*, "Intensity interferometry measurements with hard x-ray fel
pulses at the linac coherent light source", in "X-Ray Free-Electron Lasers: Beam Diagnos-
tics, Beamline Instrumentation, and Applications II", vol. 9210, p. 92100M (International
Society for Optics and Photonics, 2014).

Spence, J., "Xfels for structure and dynamics in biology", IUCrJ 4, 4, 322–339 (2017).

Trost, F., K. Ayyer and H. N. Chapman, "Photon statistics and signal to noise ratio for inco-
herent diffraction imaging", New Journal of Physics 22, 8, 083070, URL https://doi.org/
10.1088%2F1367-2630%2Faba85c (2020).

Trost, F., K. Ayyer, D. Oberthuer, O. Yefanov, S. Bajt, A. Weimer, A. Feld, H. Weller,
S. Boutet, J. Koglin, N. Timneanu, J. von Zanthier, R. Röhlsberger and H. Chapman,
"Speckle contrast determination of x-ray fluorescence for short exposure times and fluctu-
ating intensities", Journal of Synchrotron Radiation [Manuscript submitted for publica-
tion] (2022).